2020

OPTICAL SPECTROSCOPY AND THEORETICAL MODELLING OF CARRIER DYNAMICS IN GROUP-IV ALLOY QUANTUM DOTS

Rahnuma Rahman
Virginia Commonwealth University

OPTICAL SPECTROSCOPY AND THEORETICAL MODELLING OF CARRIER DYNAMICS IN GROUP-IV ALLOY QUANTUM DOTS

A thesis submitted in partial fulfillment of the requirements for the degree of Master of Science at Virginia Commonwealth University

by

Rahnuma Rahman

Bachelor of Science, Bangladesh University of Engineering and Technology, 2015

Supervisor: Ümit Özgür, PhD

Professor

Department of Electrical and Computer Engineering

Virginia Commonwealth University
Richmond, Virginia
July 2020

Acknowledgement

I would like to express my gratitude to my advisor, Professor Dr. Ümit Özgür. It has been a pleasure to have been guided by him. I am thankful to him for not only providing me with valuable ideas but also for his exceptional ability to interpret any complex topic with simplicity. Without his invaluable help, guidance, encouragement and most importantly his endless patience, this thesis would not have been possible. I am also thankful to him for all the efforts that he has made for my personal development as a researcher. I would like to acknowledge Professor Dr. Vitaliy Avrutin and Dr. Nathaniel Kinsey for all the helpful comments, critiques, and guidance throughout my education period here at VCU and with my research. I would also like to thank my research colleagues for their invaluable conversations, camaraderie, and friendship. I would like to specifically thank Md. Ataul Mamun, Rezwan Mohammad Sayeed, Benjamin Horstmann, Dhruv Fomra, Ray Secondo and Dr. Kai Ding. Additionally. I would like to thank all of those that I have found friendship with during my time at VCU. Lastly and most importantly, I would like to thank my parents and my family for their unending support and encouragement.

Table of Contents

List of Figures

List of Tables

Abstract

OPTICAL SPECTROSCOPY AND THEORETICAL MODELLING OF CARRIER DYNAMICS IN GROUP-IV ALLOY QUANTUM DOTS

By Rahnuma Rahman

A thesis submitted in partial fulfillment of the requirements for the degree of Master of Science at Virginia Commonwealth University

Virginia Commonwealth University, 2020.

Major Director: Ümit Özgür, Ph.D.
Professor
Department of Electrical and Computer Engineering

In recent years, $Ge_{1-x}Sn_x$ alloy quantum dots (QDs) have attracted significant interest due to their potential applications in photodetectors and light emitting devices in visible to mid IR spectral range and compatibility with silicon based platforms. While bulk Ge is an indirect bandgap semiconductor (0.66 eV), direct transitions can be made possible by incorporation of α-Sn at concentrations of ~10%, which however lowers the bandgap. Utilizing quantum confinement by reducing the size to below the Bohr radius also promotes direct transitions and more importantly increases the fundamental transition energies in GeSn alloy QDs, making them suitable for a variety of optoelectronic applications. The emission energy of the GeSn alloy QDs can be tuned (1.31eV to 2.0 eV) by changing the size as well as varying the Sn composition. Incorporation of α-Sn is also predicted to increase the transition oscillator strengths in both GeSn bulk and GeSn alloy QDs, and therefore, enhance radiative recombination rates. Colloidal synthesis, which is used here to realize the GeSn QDs, provide the added advantage of being a facile, low cost approach to production of alloy QDs that can be passivated with different types of ligands via solution processing to enhance emission and change emission wavelength.

Variation of size and alloying with Sn impacts carrier dynamics by changing the bright and dark exciton splitting energy and recombination pathways in the colloidal GeSn QD system. As a result, the ultra-small QDs (size equal to or less than 2nm) exhibit a distinct characteristic of blue shift in peak photoluminescence with increasing temperature. Larger size QDs (~4nm) on the other hand show little to no shift in PL peak emission with temperature. In this thesis, temperature dependent steady-state photoluminescence (PL) and time-resolved photoluminescence (TRPL) measurements were performed on ultrasmall (~2nm) and larger size (~4nm) QDs with varying Sn content (up to 6%) to reveal the underlying size and composition dependent physical properties that govern the carrier dynamics of the system. A rate equation model was developed considering the temperature dependences of excitonic levels, trap state densities, carrier transfer between excitonic and trap states, and radiative and non-radiative recombination to fit the integrated PL intensity and peak PL energy dependences on temperature.

The model shows that there is an increase in surface trap state density with decrease in QD size and increase in Sn content. Smaller QDs show larger changes in excitonic levels with temperature which causes a steady increase in PL peak emission for ultra-small QDs from 15K to 300K. There is also activation of bright excitons which dominate higher temperature PL peak emission while lower temperature PL peak has significant contribution from trap states and dark excitons. These dependences explain the observed steady increase in PL peak emission for ultra-small QDs and the drastic reduction of PL decay time from μs to ns range indicating gradual activation of bright excitons with increasing temperature from 15 to 300 K. On the other hand, for larger QD's the exciton splitting is smaller and there is little change in the excitonic levels with temperature causing the PL peak emission to show negligible change with change in temperature. The model also shows that, the non-radiative channels activate at lower energies when there is significant

increase in Sn content for QD's with comparable sizes and exciton binding energy stays more or less independent of Sn composition.

Although GeSn QD system can span the spectrum from the visible to near-IR region, to extend the spectral coverage to shorter wavelengths (UV) alloying with Si can be employed. This thesis also explores GeSiSn alloy QD system using PL and TRPL studies. Introducing Si changes excitonic dynamics in the GeSiSn system with the decay time staying in ns range for the whole temperature range (15-300 K). Extension of the rate equation modelling is used to determine the luminescence mechanisms of the system and the temperature independent decay time is understood to be due to significant lowering of the dark-bright exciton splitting energy with Si incorporation. These investigations into changes in optical properties, carrier relaxation and recombination processes with change in size and composition is crucial to designing future efficient optoelectronic devices based on abundant group IV elements.

Introduction

Among alternative materials that can be explored for application in optoelectronic devices, Silicon and Germanium draw substantial attention. These group IV elements are found in abundance in nature, are low cost, non-toxic and have well established existing processing technologies. Group IV materials are used in many optoelectronic devices like photodetectors, light emitting diodes, photovoltaics and imagers [1-7] and in recent years, the wavelength range of operation for these devices have been extended to the mid and long-wave infrared (IR) regions. Light absorption cross section and emission efficiency from these devices however suffer from major limitation as it has indirect nature of the bandgap (Ge bandgap 0.67 eV). Indirect semiconductors have relatively low optical transition probabilities as the momentum conservation for radiative recombination requires the involvement of phonons.

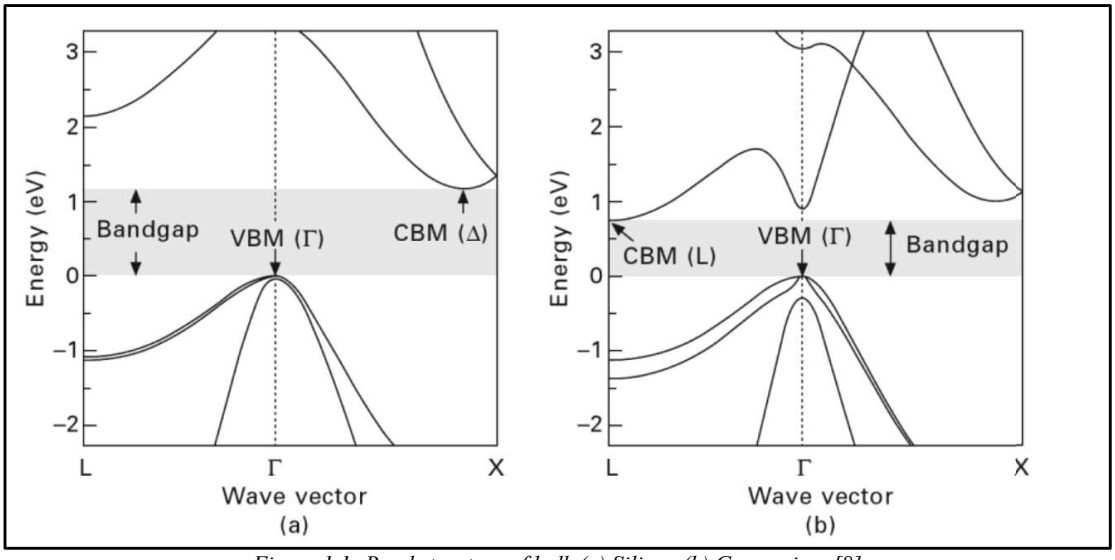

Figure 1.1: Band structure of bulk (a) Silicon (b) Germanium [8]

There are number of methods that have been explored to achieve direct transition in Germanium over the years such as application of mechanical stress [9-11], heteroepitaxial growth [12, 13] and incorporation of α-Sn and Silicon [14-17] . Density functional theory (DFT) calculations performed by Gupta et al. and Yin et al. predict that 8% and 6.3% Sn content respectively, can cause the indirect to direct band gap crossover in GeSn alloys [18, 19].

Photoluminescence study of strain free-GeSn layers suggest that direct gap transition occurs at 6–8% Sn [20, 21]. α-Sn incorporation also increases electron and hole mobility which can be useful in fabrication of high-speed optoelectronics [22, 23]. However, α-Sn (0.08eV) incorporation lowers the bandgap of the alloyed Ge and Sn system and promotes metallic character. This in turn limits spectral range of the devices based on GeSn alloys to the IR spectral range. To circumvent this lowering of bandgap, quantum confinement can be utilized. In fact, by using structures that utilize quantum confinement such as quantum wires [24] and quantum dots [25], the spectral range of alloyed GeSn system has been extended to visible.

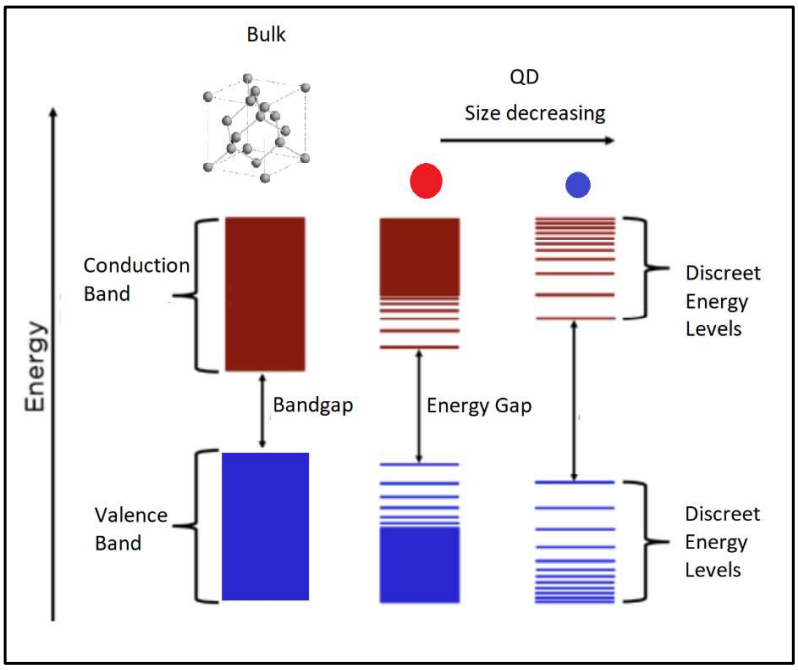

Figure 1.2: Change in band structure due to quantum confinement

Semiconductor quantum dots (QDs) are lucrative as they can allow for wider bandgap tunability in addition to enhanced optical efficiency. This is a direct consequence of quantum confinement which originates from reduction in the size from bulk to that below the exciton Bohr radius of the material. Emission energy and probability of radiative transition hence can be tailored by changing the size of the nanoparticles. In quantum confined regime, effective mass approximation can be used to determine the change in energy gap for the nanocrystals given by

the following formula [26],

$$\Delta E = \frac{\hbar^2\pi^2}{2R^2}\left(\frac{1}{m_e^*}+\frac{1}{m_h^*}\right) - 1.786\frac{e^2}{\varepsilon R} - 0.248E_{Ry}^* \quad \ldots\ldots 1$$

Here, m_e^* and m_h^* are effective masses of electrons and holes, R is the nanocrystal cluster radius, ε is the dielectric constant and E_{Ry}^* is the effective Rydberg energy

Colloidal synthesis of quantum dots offers additional advantages as they are low cost, solution processed routes of quantum dot synthesis. Quantum dots are prone to defects at surface which hinder radiative recombination. Passivation with different types of organic molecules are routinely used to enhance emission and quantum yield of the QD[27, 28]. Passivation can also alter emission characteristics in certain QD systems and even shift the emission wavelength[29, 30]. Colloidal synthesis also offers easy passivation of surface via wet chemistry. Colloidally synthesized ultra-small GeSn QDs with sizes as small as 2 nm have recently been reported. These QDs have composition tunable energy gaps from visible to near infrared [31, 32]. In these ultra-small $Ge_{1-x}Sn_x$ QDs, quantum confinement allows highly efficient optical transitions. Steady state photoluminescence (PL) of the QD's show that, by varying Sn content between 5% to 23%, energy gaps can be varied from ~2eV to 1.72eV [33]. TRPL studies show, slow decays on the order of μs at 15K and ns at 300K for the photoexcited carriers in these QDs. Theoretically, the slow decay is explained to be a result of radiative recombination of spin-forbidden dark exciton and from carriers at surface traps. At high temperature, with additional thermal energy, these excitons can transition to a spin-allowed bright state and recombine radiatively with short decay time on the order of ns. α-Sn also enhances the oscillator strength in Ge QDs enhancing radiative transition rates and causes blending of excitonic states[32] which gives GeSn quantum dots great potential as emitters in different optoelectronic applications. The temperature dependent steady state PL studies show a blue shift in PL peak emission for the ultra-small QDs. To further extend the spectral coverage

to UV range, Si can be incorporated into the alloy system.

In this thesis, $Ge_{1-x}Sn_x$ quantum dots that are of size ~2 nm QDs (Sn content 6.6% and 5.5%) and 4 nm QDs (Sn content 2.4% and 5.9%) have been investigated using solid state photoluminescence and time resolved photoluminescence. 2 nm size QDs show clear blue shift with increase in temperature of around 55 to 60 meV. 4 nm QDs do not exhibit any perceptible shift with temperature. To interpret these experimental observations, a rate equation based model has been explored in this thesis. This model considers the bright, dark and trap states in QDs and change in carrier distribution between these states with change in temperature. To explore possibility of extending spectral coverage towards UV, GeSiSn alloy QD system is investigated which shows ns decay in both low and high temperature regime. The model is then extended to the ternary alloy system to differentiate between the temperature dependent decay characteristics of the binary and ternary QD alloy system.

The discussion in this thesis will be distributed over several chapters to introduce and sequentially explore the large topics of excitonic splitting (dark and bright states), change in splitting due to temperature, carrier distribution between excitonic and trap levels through interactions with phonon, and finally change in emission energy and PL quenching of group IV alloy QDs. The first chapter discusses the overall motivations of utilizing the group-IV binary and ternary QD material system, spectral coverage with change in size and composition, possible methods of extension of operational spectrum and the challenges that will likely arise in practical implementation of the QD system. Next chapters will focus on previous work done on this GeSn alloy. This will transition into detailed discussion about recent experimental results, the theoretical model being explored and a discussion of the physics governing the behaviors observed. This thesis in short, will consider exciton splitting, trap state distribution and overall energy landscape of quantum confined group IV alloys and then introduce a theoretical modelling to further explain

the PL behavior with change in temperature and explain the carrier dynamics. Once that background has been laid out, the mathematical model is used to derive a correlation is developed between the key parameters of the theoretical model and physical phenomenon occurring in the QD system.

2. Optical Properties of GeSn Alloy Quantum Dots

2.1 Background

Silicon (Si) and Germanium (Ge) is a group IV non-toxic material and are found in abundance in nature. Both bulk Ge and Si have indirect bandgaps, that is the minimum of their bandgap is not located Γ valley and radiative recombination of carriers requires phonons for momentum conservation. However, if the materials can be made direct by engineering its bandgap, it can unlock useful new properties that can find applications in different kinds of optoelectronic devices spanning the UV to infrared spectrum. In the past few years, different methods have been explored experimentally to engineer the bandgap of group IV materials and make them direct. In Ge, since the Γ valley and L valley separation is quite small (140 meV), application of tensile strain can lower the L valley minima making it direct. Application of tensile strain can be achieved in several different methods such as micromechanical strain application on bulk germanium or via the method of epitaxial growth of Ge on larger lattice constant buffer layers etc.

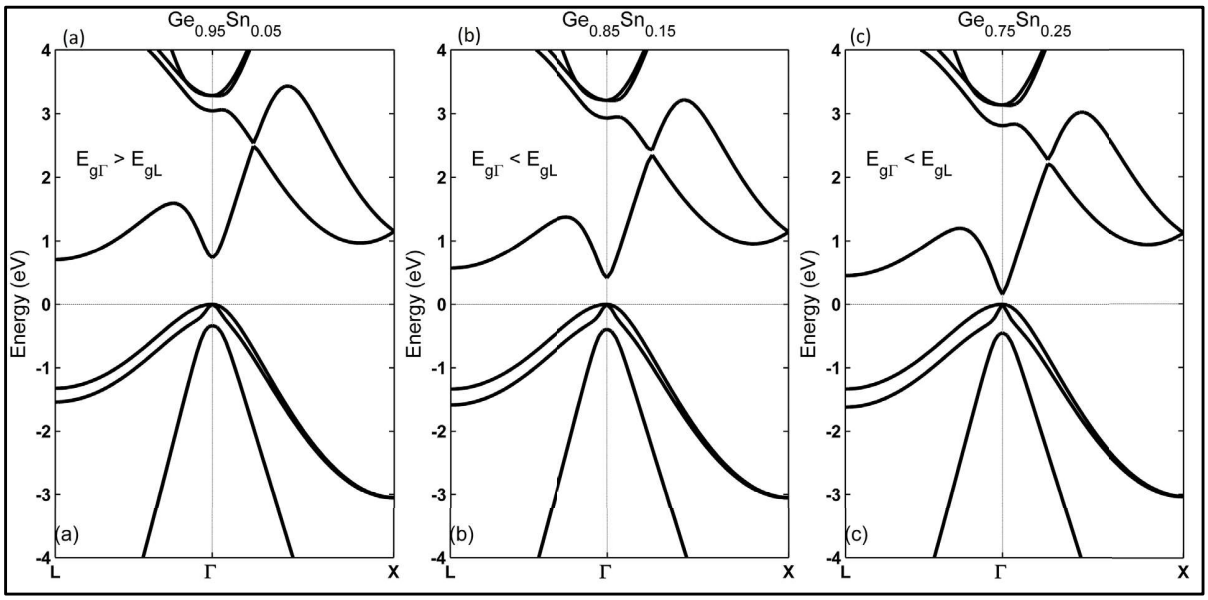

Figure 2.1. Calculated band structure for GeSn alloy with (a) 5% Sn, (b) 15% Sn, and (c) 25% Sn. [17]

One other method is alloying with material with lattice constant mismatch like Germanium or

Silicon. Lattice constant of Ge is 5.65 Å. α-Tin (Sn) is good conductor that has lattice constant of 6.489 Å. As a result of alloying these two materials, the lattice constant changes because of tensile strain which in turn changes the bandgap to make it become more and more direct. It has been demonstrated that at around 6% to 10 % Sn integration with Sn [34], Ge tends to become quasi-direct [15, 16]. It has also been observed that α-Sn incorporation tends to increase mobility of the holes and electrons in GeSn alloy making it suitable for high speed applications. The alloy thus shows tremendous potential as a light emitting devices. These advantages are amplified manifold by the ease of integration with silicon platforms in Ge based devices at low cost [35].

The bandgap of Sn itself is on the lower side (0.08 eV), so although incorporation with Sn tends to make the alloy quasi-direct, it lowers the bandgap and puts a limit on access spectral bandwidth. One way to gain access to broader range can be done by utilizing quantum confinement by shrinking the size of the alloy from bulk to quantum dots (QD). Confinement offsets the effect of alloying as it tends to increase the energy gap. So, instead of using bulk Germanium, a better approach is to use GeSn alloy quantum dots. Also, at size scales that are smaller or comparable to bulk Bohr radius of the semiconductor [36, 37], the overlapping of electron hole wave functions result in discrete energy levels like atoms. This in turn enhances the efficiency of the radiative recombination manifold compared to alloyed bulk counterparts. Theoretical first principles calculations have also shown that, α -Sn incorporation increases the oscillator strength to the GeSn quantum dots mixing the bright dark exciton states [32]. GeSn quantum dots thus have potential as good emitters in different optoelectronic applications.

Quantum Dots can be made in several ways. Some notable methods are molecular beam epitaxy, chemical vapor deposition or colloidal chemistry. Colloidal synthesis is both low cost and easy to implement wet chemical method. It also provides an easy route of ligand passivation for the synthesized quantum dots and can be later drop cast onto different substrates. Ligands are a

key parameter when preparing nanomaterials by wet chemical precursors; It can function primarily as a stabilizing agent, providing colloidal stability, stopping uncontrolled growth and agglomeration. The ligands control the rate of growth, particle morphology, reaction pathways and the particle size distribution. At a deeper level, the electronic structure of the passivating ligands contributes to the overall electronic and optical profile of the nanoparticles, blocks surface states and hence has a direct effect on emission yields [38]. In certain QD systems it can even alter the emission characteristics. Some QDs like Si nanoparticles are especially prone to oxidation so ligand passivation is routinely used to enhance emission and stop degradation of the QD over time [39].

There are several drawbacks that tend to make the successful implementation of GeSn QD's in different applications difficult. Sn is a large atom and puts significant strain around the lattice site where it substitutes Ge atoms causing the lattice constant to increase. This effect is significant and influences bandgap of GeSn alloy quantum dots to a great extent making the energy gap lower. It also increases disorder in the system. In the exceedingly small (less-than ~2 nm) size QDs, the ligands are at times not able to passivate all the free surface states. This is because the size of the ligands are usually large as they are organic long chain molecules. A loss of emission is observed at sizes of around 5-10 nm. This can be due to loss in quantum confinement which causes lowering of the energy gap. This lowering of energy gap when coupled with remaining defects and thermal variations can cause complete quenching [40] of any radiative recombination. Also, the highest transition energy with ultra-small dots have been around 2eV with Sn incorporation of 5.5%. To extend the coverage of the GeSn QD, another method can be incorporation of Silicon into the system to make a ternary alloy system.

Moontagroon et. al [15] reports that the direct gap ranges from 0.70 to 0.95 eV can be achieved in bulk SiGeSn alloy by varying the composition of Silicon and Sn. Lattice parameter of silicon

(5.43Å) is less than Ge and Sn and alloying can cause compressive strain which can shift the bandgap to higher energy. Quantum confined GeSiSn QDs can thus expand spectral coverage to the short UV wavelength range giving larger control over tunability via both size and composition.

2.2 Previous Work

GeSn bulk and GeSn thin films area well explored system. $Ge_{1-x}Sn_x$ alloys thin films have been produced via chemical vapor deposition and molecular beam epitaxy and demonstrate tunable band gap energies in the mid-IR region [41, 42]. There are, however, challenges associated with this as growth of homogenous thin films. They tend to show phase segregation during high temperature growth process due to poor crystallinity and show increased presence of high density of defects in case of low temperature growth [43].

To this end, colloidal synthesis has demonstrated high quality, solution processable $Ge_{1-x}Sn_x$ QDs while avoiding phase segregation of Sn. Before the samples measured in this research, the synthesis of phase-pure $Ge_{1-x}Sn_x$ nanoalloys with sizes in the range of 15 −23 nm and 3.4−4.6 nm with Sn compositions up to x = 0.279, have been demonstrated [31].

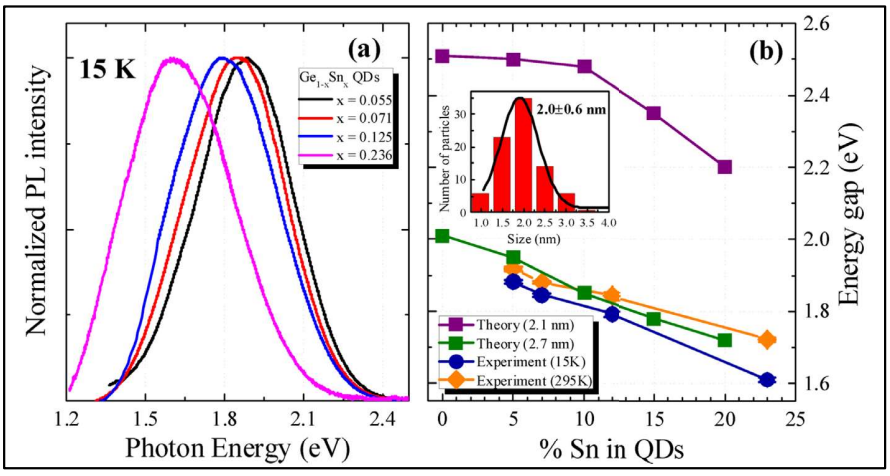

Figure 2.2: PL spectra of $Ge_{1-x}Sn_x$ QDs with varying Sn content at 15 K, (b) experimental (PL peak) and theoretical energy gaps as a function of Sn concentration in 2.1 and 2.7 nm QDs. Inset shows the size histogram of $Ge_{0.77}Sn_{0.23}$ QD sample, representative of QDs with different Sn compositions, obtained from TEM analysis with no post synthetic size selection. [33]

Ultra-small QDs have also been explored to investigate the full extent of quantum

confinement in GeSn QDs with size 2.0±0.7 nm and Sn compositions of x = 0.05, 0.07, 0.12, and 0.236 (Figure 2.2). These particles retain their diamond cubic structure and have homogeneous distribution of Ge and Sn. The GeSn alloy QDs have the same average particle size and spherical morphology, hence the systematic red-shift (1.88 to 1.6 eV at 15K) in PL can be attributed to the decrease of bulk bandgap due to increasing Sn content. As the gaps of $Ge_{1-x}Sn_x$ QDs are well above those of their bulk counterparts (0.1- 0.6 eV) [44], it is clear indication of strong quantum confinement effects in this ultrasmall size regime. The theoretical energy gaps calculated using tuned HSE for 2.1 and 2.7 nm size GeSn QDs are plotted alongside the low and high temperature peak positions in Figure 2.2 with change in Sn content. Experimentally obtained band-gaps are consistent with theoretically calculated values for 2.7 nm QDs. The deviation from 2.1nm size can be attributed to a combined effect of the size variation in the sample and PL from larger size dots in the sample dominating radiative recombination due to better passivation. The PL peak positions are also significantly blue shifted in room temperature compared to low temperature. This temperature dependence shift in peak emission energy from QD could be due to the interplay between excitonic states.

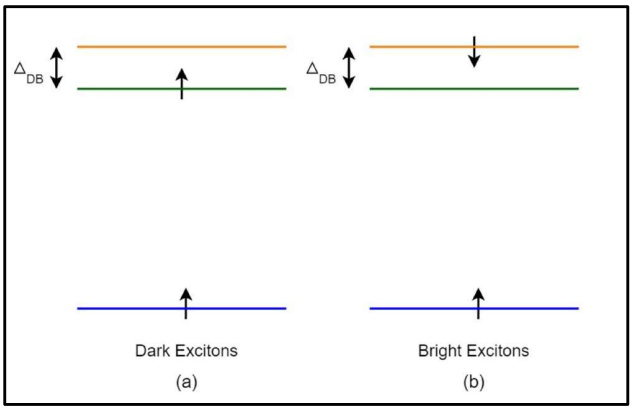

Figure 2.3: Dark excitons (left) are optically forbidden and Bright excitons (right) are optically allowed. Bright and dark excitons can have different spin arrangements ('up' or 'down')

Excitons have significant effect on the optical properties of semiconductors. Excitons are electron–hole pairs that are bound by Coulomb interactions. Depending on the orientation of

the spin, excitons can be bright or dark. In bright excitons, spins of electron and hole are anti-parallel and radiative transitions are allowed through photon emission. In dark excitons, the spins are parallel hence radiative recombination requires spin flip for spin-momentum conservation. As a result, bright excitons have higher probability of recombination, shorter lifetime (ns) and hence are considered optically active. Dark excitons have low transition probability as they require spin-flip, have long decay time in the order of μs and are considered optically inactive or dark. Electron-hole exchange interaction causes there to be energy difference or splitting to exist between dark and bright exciton states (Δ_{DB}). Quantum confinement effect enhances the electron-hole exchange interaction and as a result the splitting observed in semiconductor nanocrystal is generally large compare to bulk semiconductors. In bulk II–VI semiconductors, splitting as low as 0.13 meV (CdSe) have been reported[45]. On the other hand, Δ_{DB} can be in the order of few meV to several tens of meV [46, 47] depending on the QD system, size and composition. At low temperatures, excitons in the QDs occupy the lower-energy dark states and as the temperature increases, thermal activation of bright exciton takes place and consequently PL emission blue-shifts to higher energy. Temperature dependent photoluminescence studies on these sample samples showed fast ns decay at room temperature and slow decay in μs range for the lower temperature regime which is consistent with the excitonic carrier dynamic.

The decays were obtained in this work were obtained by fitting to a biexponential model given by,

$$A_{fast}e^{-\frac{t}{\tau_{fast}}}+A_{slow}e^{-\frac{t}{\tau_{slow}}}.$$

Ultra-small QDs are harder to passivate and hence can contain large number of surface defects. Two-component PL decay is observed where non-radiative surface recombination is present

which is faster than radiative decay [48] as can be seen in Figure 2.4. τ_{slow} remains in the range or around 10 ns for QDs with Sn content up to 12% and 28 ns for the QD sample with 23% of Sn. At low temperature, τ_{slow} (~ 24 μs) is showing no dependence on the Sn content

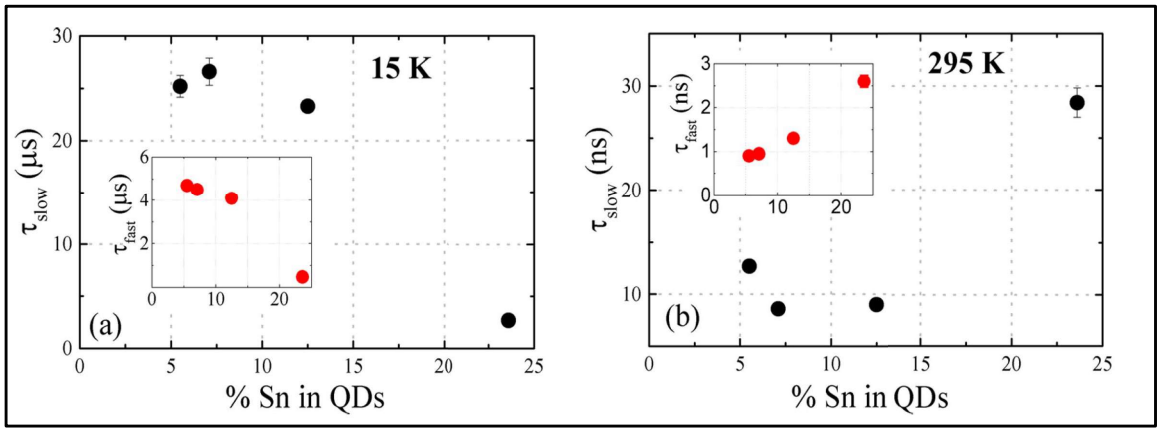

Figure 2.4: PL decay times measured at (a) 15 K and (b) 295 K as a function of %Sn in $Ge_{1-x}Sn_x$ QDs. Fast decay components are shown in the insets of (a) and (b) [33]

for up to 12 % Sn but decreases significantly to 3 μs for 23% Sn. The room temperature decrease in PL decay time is indicative of activation of bright exciton states. Theoretically the decay time at room temperature is expected to be around 10-20ns showing very weak decrease with increase in Sn content. The dark excitons should have a theoretical lifetime of ~1-10 μs with slight increase up to 5% Sn incorporation. The significant change at 23% indicates surface states that contribute to radiative recombination with slow decay. At low temperatures, carriers could be localized at the surface, with small overlap between the wavefunctions and these carriers could account for almost no change in PL lifetime up to 12.5% Sn.

Another study by the same group has explored larger size $Ge_{1-x}Sn_x$ alloy quantum dots (QDs) with variation between 3.3±0.5 to 5.9±0.8 nm. The Sn composition was varied from (0–20.6%), and which leads to near infrared (IR) photoluminescence (PL) and tunable energy gap. Linear expansion of cubic Ge lattice with increasing Sn was observed that indicated stress free formation of nanoalloys. Energy gaps were significantly blue shifted from bulk Ge (0.67eV) for $Ge_{1-x}Sn_x$ alloy QDs because of quantum confinement.

Table 1: *Comparison of the elemental composition, crystallite and primary particle size, and room temperature solid state absorption onsets and photoluminescence peak energies for 3.3 ± 0.5 – 5.9 ± 0.8 nm $Ge_{1-x}Sn_x$ alloy QDs.[40]*

Sample	Sn Composition (x)[a]	Particle Size (nm)[b]	Crystallite Size[c] (nm)	Energy gap (eV)[d]	PL Peak Position (eV)
1	0.015	3.3 ± 0.5 nm	1.9 ± 0.2	1.72	1.62
2	0.019	3.4 ± 0.5 nm	2.1 ± 0.2	1.61	1.52
3	0.027	3.5 ± 0.6 nm	2.2 ± 0.2	1.52	1.43
4	0.034	3.7 ± 0.5 nm	2.4 ± 0.2	1.48	1.38
5	0.042	3.9 ± 0.6 nm	2.8 ± 0.2	1.30	1.34
6	0.056	4.4 ± 0.7nm	2.8 ± 0.2	1.22	1.31
7	0.064	4.5 ± 0.6 nm	2.9 ± 0.2	1.02	n/a[f]
8	0.079	4.6 ± 0.8 nm	3.0 ± 0.3	0.94	n/a[f]
9	0.091	5.0 ± 0.7nm	3.3 ± 0.2	0.84	n/a[f]
10	0.112	5.2 ± 0.6 nm	3.5 ± 0.3	n/a[e]	n/a[f]
11	0.154	5.5 ± 0.8 nm	3.6 ± 0.3	n/a[e]	n/a[f]
12	0.206	5.9 ± 0.8 nm	3.8 ± 0.2	n/a[e]	n/a[f]

[a]Elemental compositions of Ge and Sn were obtained from SEM/EDS analysis of multiple individually prepared samples and the averaged values obtained from 5 individual measurements for each sample are presented. [b]Average particle sizes were calculated from 150−200 individual QDs from TEM images of multiple individually prepared samples. [c]Crystallite sizes were calculated by applying the Scherrer formula to (111), (220), and (311) reflections of PXRD patterns and average values are presented. [d]Energy gaps were estimated from extrapolating the first major absorption onset to the intersection point of the baseline using linear fits. [e]Onset cut off due to detector limitation. [f] No detectable PL was noted.

Table 2.1 lists the change in PL peak position observed with change in QD size and composition (Sn concentration). The PL peak energy varies in the near-IR with change in composition. In this study, the reported PL peak and absorption onsets were found to be remarkably close to each other which is indicative of energy gap transition. As can be noted here, PL from larger dots are not discernible in this study for samples with Sn content higher than 5.6%. Poor surface passivation couple with weaker confinements because of increase in nanoparticle size, could lead to large numbers of non-radiative recombination that can lead to loss of luminescence. Carrier relaxation was again explored through TRPL at low and high temperatures for $Ge_{1-x}Sn_x$ QDs with Sn composition 1.9%, 4.2% and 5.6%. Biexponential fits like the one

previously mentioned revealed again fast decay in the order of 8 ns -11.7 ns and 80 ns -119 ns at room temperature. Low temperature decays were in the order of 1-2 μs and 8-11μs.

In this thesis, carrier dynamics in ultra-small (~2nm) and larger (~4nm) GeSn QD systems are explored using temperature dependent steady-state and time-resolved photoluminescence. Changes in PL peak position and decay times with temperature for QD samples with varying sizes and compositions are investigated. The temperature dependent changes in decay time, Pl peak energy and integrated Pl intensity are explained using a rate equation modelling considering the change in exciton splitting with temperature as well as carrier redistribution between bright, dark excitonic states and trap states.

3. GeSn Alloy Quantum Dots: Modeling of Carrier Dynamics and Study of Steady-State and Time-resolved Photoluminescence with Size and Composition Variation

GeSn quantum dot is an interesting alloy QD system due to its innate compatibility with existing silicon platforms. There is the additional advantage due to QD systems having inherent size tunable radiative transition and increased oscillator strength as a direct consequence of incorporation of α-Sn. To utilize this system to unleash its full potential for, a complete understanding of excitonic dynamics, distribution of carrier populations after excitation, effect of trap states and effect of temperature on the overall performance of the QD system is necessary.

In this chapter, temperature dependent steady-state and time-resolved PL measurements on the GeSn QD system are discussed first. In the subsequent section, a rate equation model is introduced to explain the observed experimental behavior. This theoretical model aims to establish a correlation between carrier dynamics involving trap states and excitonic states via absorption and emission of phonons while considering the change in excitonic splitting energy that may occur with change in temperature. The following section will draw comparison between the experimental data and the theoretical estimates to further elucidate the physical significance of the parameters defined in the model.

3.1 Temperature dependent steady-state and time-resolved PL measurements:

Change in carrier dynamics and emission characteristics in $Ge_{1-x}Sn_x$ QDs were explored using steady-state photoluminescence (PL) and time resolved photoluminescence (TRPL). $Ge_{1-x}Sn_x$ QD samples were produced by colloidal synthesis using high boiling alkylamine/alkene solvents and high temperature coreduction of halides in high boiling temperature [49]. The colloidal samples were drop cast onto sapphire or silicon substrates for optical measurements. The samples

investigated had 5.5% and 6.6% Sn for the ultra-small (2 ± 0.7nm sized) quantum dots and 2.4 and 5.9% Sn for the (3.7 ± 0.4 nm sized) larger size quantum dots. The steady-state PL measurements were performed by using a frequency doubled Ti: Sapphire laser with 386 nm wavelength, 150 fs pulse width, and 8kHz - 80 MHz repetition rates. To prevent degradation of the sample, the power of the incident laser radiation was kept at 1-3mW (at 80 MHz repetition rate) with the laser focused to a spot size of 100 microns Considering the number of atoms in 1 layer of QD (~10^{13} to ~10^{14}), this gives less than 1 photons per QD on average. The number of carriers generated is thus very low. To detect this level of intensity of emitted photons, a liquid N_2 cooled CCD camera connected to a spectrometer was used to obtain the steady-state PL spectra at different temperatures using a closed cycle He cryostat. TRPL at different temperatures were collected using the same excitation source and a Hamamatsu streak camera with 25 ps resolution.

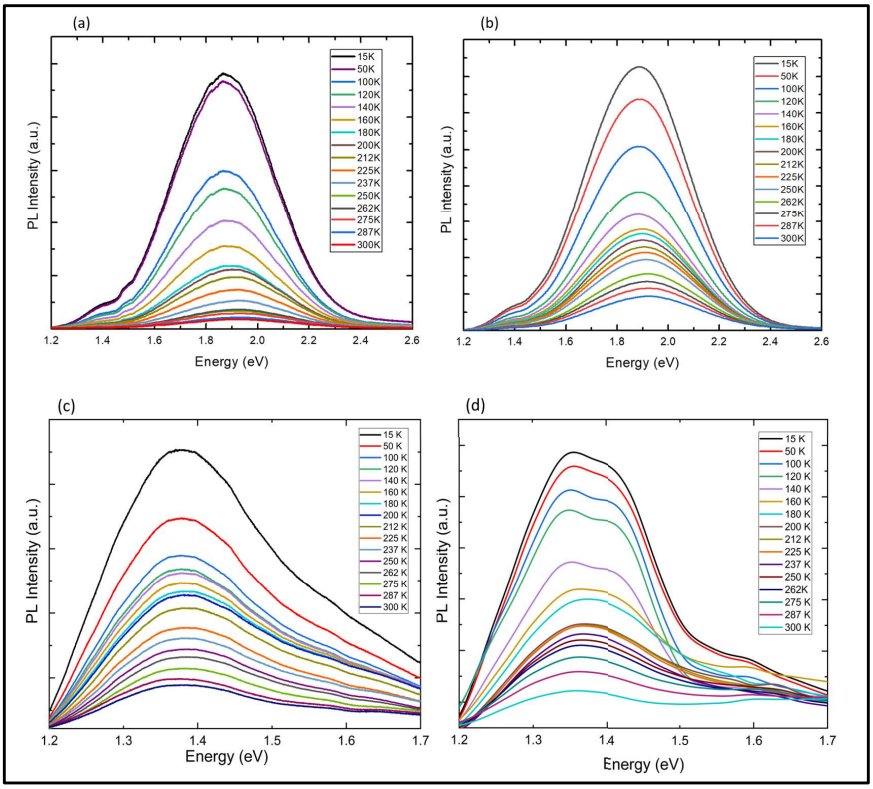

Figure 3.1: PL spectra of $Ge_{1-x}Sn_x$ QDs with varying Sn contents for temperatures ranging from 15K to 300K. (a) 5.5 % and (b) 6.6 % Sn content (~2 nm QDs). (c) (c) 2.4 % and (d) 5.9 % Sn content 4 nm QDs.

Figure 3.1 presents the solid state photoluminescence with temperature variation for the ultra-

small (~2nm) [(a) and (b)] and for the larger size (~4nm) [(c) and (d)] quantum dots. The peak emission energy shifts from visible to near infrared (1.88 to 1.37) with the increase in QD size. There is slight red shift from 1.87 eV to 1.86 eV measured at 15K with the variation in Sn content for 2nm quantum dot system. Since the size has little variation between the two samples, this can be attributed to the increase in Sn content. The 4nm quantum dots however show broad peaks and the peak position for the QD with 2.4% Sn is around 1.38±0.3 eV measured at 15K. For the 5.9% Sn composition there is competition between two pronounced peaks at 1.37eV and 1.42eV at 15K. The broader peak could be due to size dispersion where two different sizes of QD's in the sample that are luminescent at slightly different energies. Increasing Sn content is theoretically estimated to increase oscillator strength which could result in different sized QDs in the sample to have strong luminescence in the 5.9% Sn content sample at low temperature. As the temperature increases both smaller and larger size QDs show decrease in intensity of PL emission as non-radiative recombination channels are activated. This ultimately smears the two prominent peaks giving one broad peak at 300K for 5.9% Sn sample. There is also a tail observed with a peak coming up in the 4nm QD PL spectra at 1.6eV. Similar peaks and tails have been observed in other colloidal QD such as CdS with size variation between 3.1nm to 4.3nm[50]. These QD shows biexponential decay dynamic for the trap related peaks that show ns lifetime. The faster decay components show significant contribution in the larger QDs and it was attributed to the deep trap state formation following shallow trap to trap diffusion in these systems. The slower components were attributed to the emission from the deep trap states. It was also observed that there is an increase in population of deep trap states with increase in QD size. More investigation into this high energy tail is necessary to understand the overall characteristics of this emission. Systemic size dependent TRPL studies can be proposed the future to understand this observed peak.

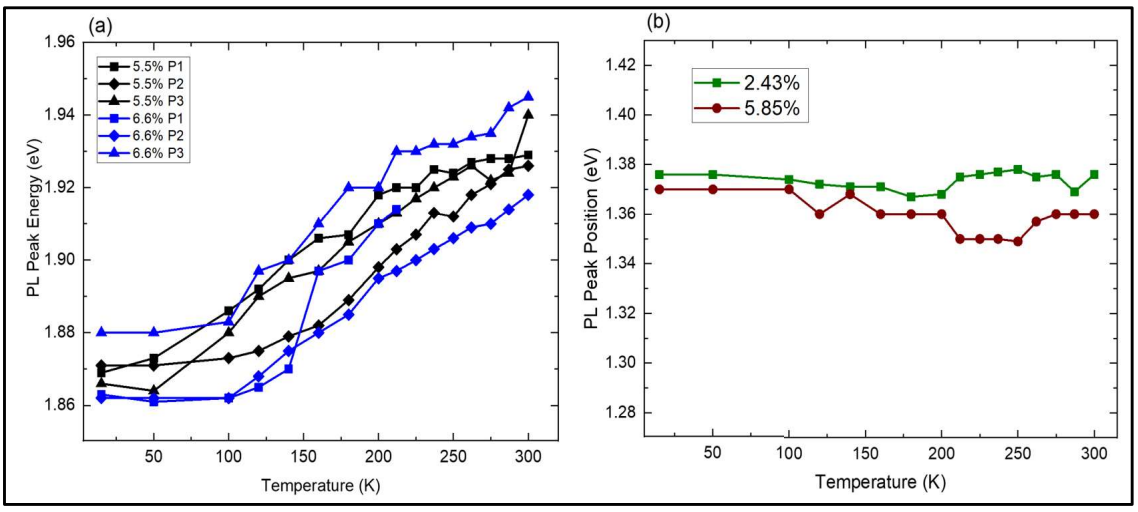

Figure 3.2: Variation in PL peak position with temperature in the (a) ~2nm ultra-small QDs with varying Sn content at different points in the samples denoted with P1, P2 and P3, and (b) ~4nm QDs with varying Sn content.

For both sizes of QDs, PL peak energies have been obtained by fitting to Gaussian functions As can be seen in Figure 3.2a, a clear blue shift of about 55-60 meV is evident for both 5.5% Sn and 6.6% Sn 2 nm QD samples as the temperature is increased from 15K to 300K. This blue shift can be attributed to the interplay between dark and bright exciton dynamics. As alluded to earlier in Section 2.2, dark excitons are optically inactive and have low probability of radiative recombination as they are spin forbidden. Bright exciton recombination is allowed and more probable due to anti-parallel spins. Dark excitons hence have longer lifetimes and are lower in energy in most quantum dots as opposed to bright excitons which have shorter lifetimes. Increased electron-hole exchange interactions cause splitting between dark and bright states often denoted by Δ_{DB}. At low temperatures, emission is dominated by the recombination of long-lived dark exciton states. As the temperature increases, carriers can be thermally excited to occupy the high energy bright exciton states leading to higher energy emission and this results in the observed blue shift. While bright exciton recombination at high temperatures enhances the radiative efficiency, increase in non-radiative recombination with temperature overcomes this enhancement resulting in an overall reduction in PL intensity as temperature increases. The previously reported experimental PL peak blueshift values range from 35meV to 110 meV [33] for 2 nm GeSn QDs

of varying Sn compositions from 5.5% to 23.6%. The samples under investigation (5.5 – 6.6 % Sn content), however, show an additional 20 to 25 meV shift as temperature changes from 15 K to 300 K. Theoretical calculations suggest a bright-dark exciton splitting value of around 50-60 meV for 2nm pure Ge QD systems (80 meV in 1.4 nm Ge QDs), and decreasing splitting with increasing Sn content. Larger than predicted shifts have been partially attributed to electron-hole radiative recombination via low energy surface states (also with relatively longer lifetime in μs range) with decreasing temperature[32]. At higher temperatures carriers can be de-trapped from the surface states and can gradually repopulate the bright states with increase in thermal energy of carriers. Low temperature radiative recombination via shallow surface trap states and gradual activation of bright exciton states with increase in temperature can account for the additional blue shift observed in the investigated samples.

The larger size quantum dots (~4nm) on the other hand exhibit no significant shift with very minor variation which is within the error margin of the Gaussian fits. A redshift of less than 10 meV can be predicted based on measurement resolution. As in bulk semiconductors, redshifts of PL peak energy have been reported in many colloidal QD systems such as CdS [51], CdSe/ZnS [52], ZnS/InP [53], Ag_2Se [54] due to energy gap lowering with increasing temperature and have been modeled using Varshni's empirical formula. With increase in size, there is possible lowering of exciton splitting level. Again, change in carrier population as temperature is increased along with lowering of bright and dark exciton level, could result in a shift that is negligible in case of the larger GeSn QDs. In the simplest picture, we consider there to be a slight energy gap shrinkage due to lattice expansion, electron-phonon interaction with increasing temperature and change in the dark-bright exciton splitting (Δ_{DB}). The observed difference in shifts in the two different sizes of QDs with increasing temperature thus can be explained using an energy level model with the excitonic levels and trap levels.

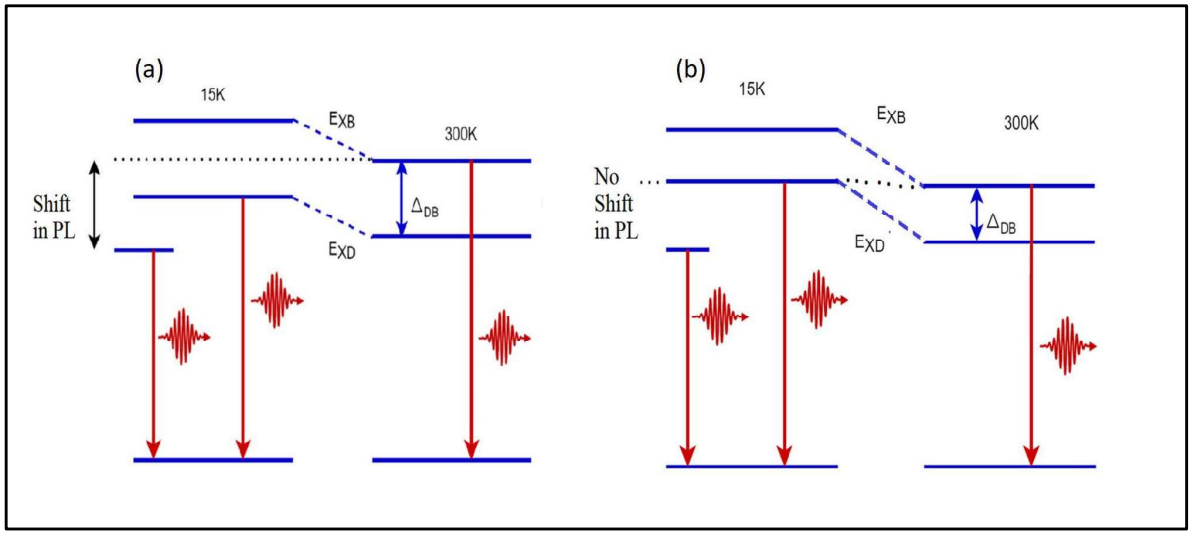

Figure 3.3: Evolution of bright (E_{XB}) and dark excitonic (E_{XD}) energy levels with temperature for 2 nm and 4 nm GeSn QDs, where the dark-bright exciton splitting (Δ_{DB}) reduces with increasing QD size. Thermal excitation of bright excitons at high temperature and trap state recombination at low temperatures results in blue shifted emission in the 2 nm QDs, but insignificant change is observed for 4 nm QDs, where the energy gap shrinkage with temperature is comparable to Δ_{DB}.

This three level energy diagram model is illustrated in Figure 3.3. As discussed in Chapter 1, ultra-small QDs are often harder to passivate with large organic ligands and thus are expected to have a larger number of surface trap states. Initially excited carriers can relax into the surface trap states along with dark states. PL at 15 K originates from radiative recombination of dark excitons and the surface trap states. With increasing temperature, while the energy gaps slightly shrink, thermal activation of higher energy spin singlet bright excitons and carrier detrapping from surface states due to thermal excitation results in a PL blueshift. On the other hand, the 4 nm QD samples do not show any discernible shift. 4nm QD's can be better passivated due to their larger size and surface area. Therefore, their surface trap state densities are expected to be lower and lower number of carriers can initially relax into those states compared to the 2 nm QDs. So, in the lower temperature regime, 4nm QDs, radiative recombination happens primarily via dark excitons. The change in energy gap with increase in temperature and exciton splitting Δ_{DB} are comparable. As a result, although bright excitons get activated and the energy levels of bright excitons at 300K is very close to the value at 15K and so, there is little to no shift observed in these samples. Interplay between the number of radiative carriers in bright, dark and trap state along with the change in Δ_{DB}

and energy gap with change in temperature, results in an observed blue shift in ultra-small QD and no shift for larger QD sizes.

Increase in PL peak energies with temperature (by 54 meV – from 0.893 eV at 10 K to 0.947 meV at 300 K) [55] has been previously reported in silicate glass samples doped with PbS quantum dots and has been attributed to two energetically different emitting states that are results of dark and bright exciton splitting and thermal energy activated interplay between them. Temperature dependence of the PL decay and integrated PL of oleic acid capped 2-3 nm PbS quantum dots [56, 57] similarly show a blue shift of around 30 meV in PL peak position with increasing temperature. Such behavior in PbS QDs has been explained using a three level system composed of bright exciton, dark exciton, and surface states, where dynamics were governed by redistribution of carriers between the dark and bright states in the low temperature regime (<180 K), by detrapping of carriers from the surface states to the dark and bright states in the intermediate temperature range (180 – 250 K) and by primarily bright exciton radiative recombination along with enhanced nonradiative processes in the high temperature range (> 250K). Using this model, a dark-bright exciton splitting energy of 3 meV was obtained, consistent with experimental expectations. Perovskites also tend to show blue shift in PL peak emission with increase in temperature in both films and in nanocrystal. Similar blue shift has also been observed in semiconductors such as copper halides (CuX, X = Cl, Br, and I) [58] and some ternary chalcopyrite containing Ag and Cu [59]. One of the largest blue shift with temperature is observed in lead halide perovskites such $CH_3NH_3PbBr_3$ perovskite QD system that shows around 150 meV shift with change in temperature 20K to 300K [60].

Different non-radiative channels are activated with change in temeprature. Along with the PL peak shift, change in the integrated PL intensity with temperature can help determine the degree of non-radiative recombination processes involved in different size and composition of the QDs.

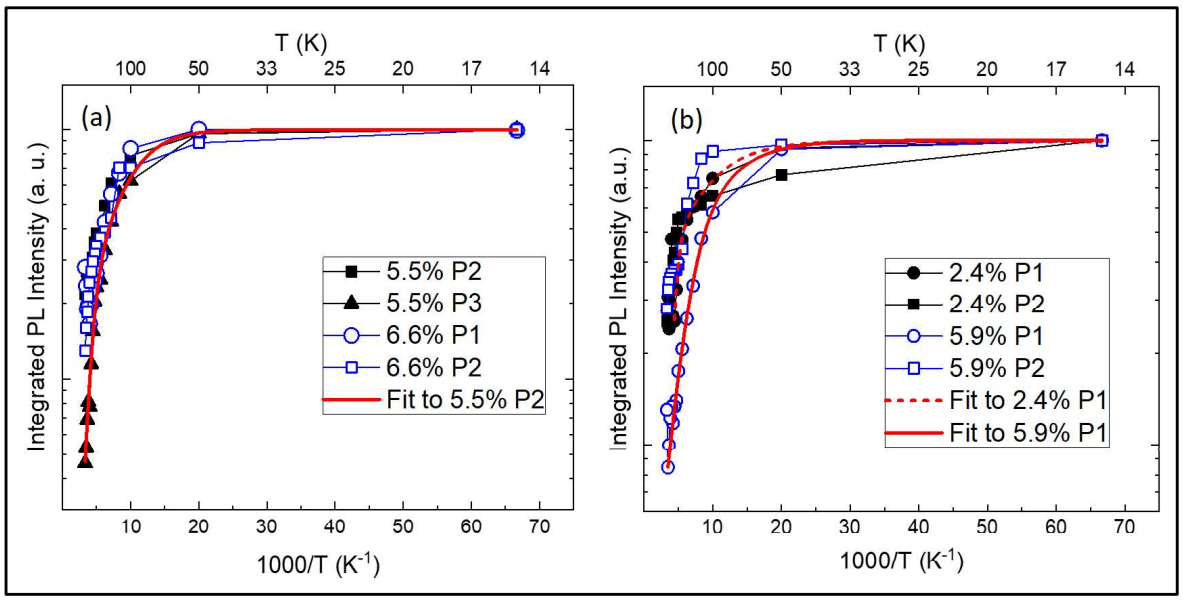

Figure 3.4: Integrated PL Intensity versus inverse temperature for $Ge_{1-x}Sn_x$ alloys for (a) 2nm QDs (b) 4nm QDs. The solid and dashed red lines are two-activation energy fits to data. P1, P2, P3 indicate different positions on the samples.

Figure. 3.4 shows swift quenching of the integrated PL intensity with increasign temperature for both 2nm and 4nm GeSn QD samples with different compositions. As the composition and the size changes, the amount of non-radiative channels present in the QD can change as well as the onset of their activation with temperature. The quenching has an onset at around 100K. The behavior of this temperature dependent quenching of the integrated PL intensity I(T) can be fitted using the following equation,

$$I(t) = \frac{I_0}{1+A_1 e^{\frac{-E_{A1}}{K_B T}} + A_1 e^{\frac{-E_{A2}}{K_B T}}} \quad \ldots\ldots (2)$$

Here, E_{A1} and E_{A2} are activation energies corresponding to two non-radiative processes, A_1 and A_2 are the corresponding amplitudes, T is the temperature, I_0 is the intensity at T = 15K, and K_B is the Boltzmann constant. Two activation energies were required for a good fit in this case. The activation energies for the 2 nm QDs do not show any significant dependence on the Sn compositions used and are E_{A1} = 25±4 meV and E_{A2} = 133±28 meV. For the 4 nm QDs, E_{A1} = 19±2 meV and E_{A2} = 185±32 meV for the 2.43% Sn content sample and E_{A1} = 17±3 meV and E_{A2}

= 52±7 meV for the 5.9% Sn content sample. E_{A1} can be considered as the binding energy associated with exciton dissociation, and E_{A2} as the thermal activation energy corresponding to the escape of carriers from quantum confinement. While there is some variation in the activation energies for a given sample, it is consistent with change in quantum confinement with QD size. In smaller QDs, the E_{A1} is higher in value. Significant reduction in the activation energy with increased size for a given Sn composition of 5-6% (from 133 meV in 2nm QDs to 52 meV in 4 nm QDs) is a possible indication of increase in amount of nonradiative centers in the cores of the larger QDs due to increased volume. As the confinement is less in larger QDs, thus the activation energy to escape the localized center is expected to be lower. It can in turn give access to more nonradiative pathways in larger QDs, reducing the activation energy. In addition, there is a significant reduction of E_{A2} with increasing Sn content in 4 nm QDs, which suggests that excitons can more easily escape from the localized core centers and transfer to nonradiative centers and/or density of non-radiative PL quenching pathways increase with inclusion of Sn. Sn has been observed to increase disorder in the alloy system[61]. QD system may not segregate due to change in colloidal synthesis method but it could still lead to increase of non-radiative pathways. The activation energy values of those reported for 2-3 nm epitaxial Ge QDs are in the range of 140 - 194 meV [62]. Slightly lower values have been reported for colloidal 2-3 nm CdTe QDs (163 - 205 meV) [63, 64]. The values obtained through the fits are hence comparable to the previously reported values in other QD systems.

TRPL were performed on the sample to gain information about the type of excitonic state taking part in radiative recombination and trap related dynamics of a system. The decay of PL intensity with time can be fitted using bi-exponential equation with fast and slow decay components as given below,

$$I_{TRPL} = A_{fast} e^{-\frac{t}{\tau_{fast}}} + A_{slow} e^{-\frac{t}{\tau_{slow}}} \quad \ldots. (3)$$

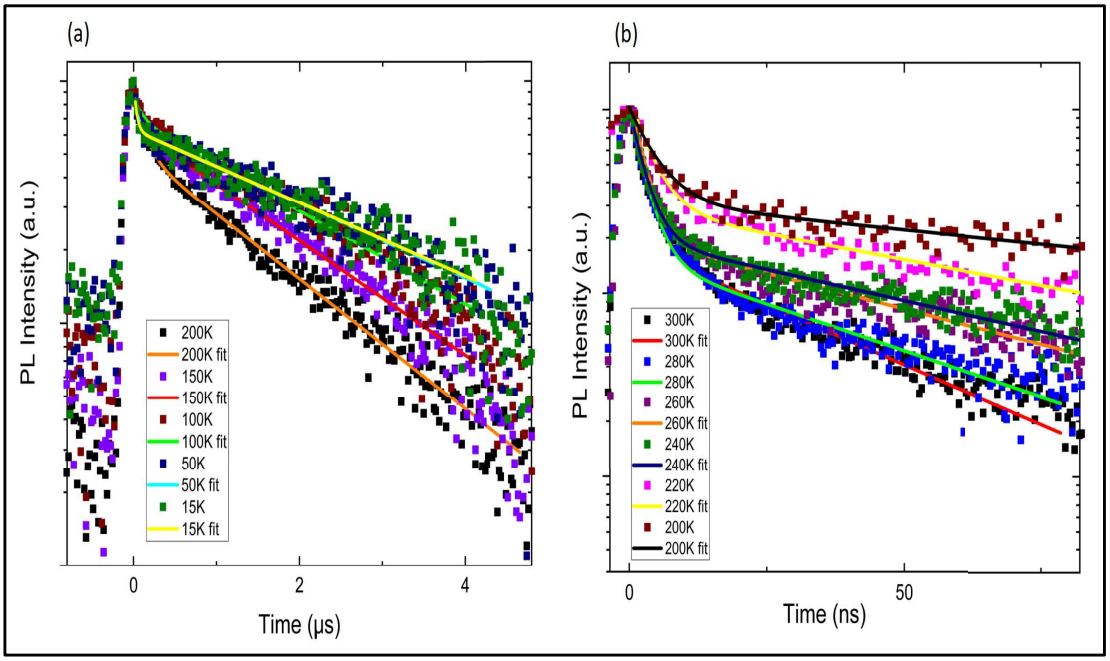

Figure 3.5: PL transients at different temperatures for the 2nm $Ge_{0.945}Sn_{0.055}$ QDs: (a) from 15K to 200 K (b) from 200K to 300 K. Note that the time window for the low temperature range is in the μs range while that for the high temperature is in the ns range. Solid lines are biexponential fits to the data.

Figure. 3.7 shows the TRPL for 2nm QD with 5.5% Sn. TRPL studies were performed for the 2nm QD with 5.5% Sn composition with temperature varying between 15K to 300K. As can be seen in the Figure 3.7,there is gradual decrease in decay times from 15 to 300 K, where the low temperature decays are in the μs range due to slowly recombining dark excitons and possibly from surface trap states, and the high temperature decays are in the ns range due to thermal activation of bright excitons. Crossover happens at around 200 to 220K region.

Table 2 lists the fast and slow decay parameters derived from fitting to equation 14,

Table 2: *TRPL decay parameters of GeSn QD (~2nm) with 5.5% Sn*

$Ge_{1-x}Sn_x$ with x% Sn		τ_{fast}	τ_{slow}	A_{fast}/A_{slow}
5.5	300K (RT)	2.48 ± 0.02 (ns)	33.22 ± 0.94 (ns)	4.5
	280K	2.63±0.06 (ns)	42.84 ± 1.56 (ns)	5.5
	260K	2.53±0.08 (ns)	56.02 ± 0.26 (ns)	5.12
	240K	2.59±0.07 (ns)	64.25 ± 1.68 (ns)	4.2
	220K	3.61 ± 0.18 (ns)	77 ± 2.74 (ns)	3.11

	200K	0.1 ± 0.01 (μs)	1.62 ± 0.025 (μs)	0.75
	150K	0.1 ± 0.01 (μs)	1.85 ± 0.02 (μs)	0.53
	100K	0.1 ± 0.04 (μs)	2.3 ± 0.04 (μs)	0.24
	50K	0.04 ± 0.0 (μs)	2.83 ± 0.07 (μs)	0.56
	15K	0.03 ± 0.01 (μs)	2.87 ± 0.07 (μs)	0.59

The A_{fast}/A_{slow} ratio shows slight increase with increase in temperature in both the ns and μs regime. However, the fast decay components significantly contribute to decay at higher temperatures. Previously, reported temporal analysis of the PL decay[33] of the same $Ge_{1-x}Sn_x$ ultra-small QD reveals a short lived higher energy PL at 295K temperature which showed insignificant contribution to overall solid state PL and was therefore attributed to the non-radiative recombination. PL decay Ge nanocrystals embedded in a thermally grown SiO_2 with size varying between 4–13 nm show fast decay component with around ~3ns lifetime[65]. The lifetime in these QD's show decreasing fast component with increasing defect density and were similarly attributed to non-radiative decay mechanisms. As temperature is increased it is possible that, activation of more and more non-radiative channels causes faster decay components to contribute more significantly to the overall PL decay hence the trend.

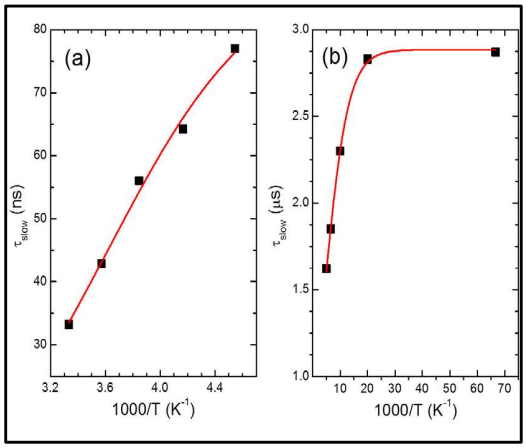

Figure 3.6: PL decay times versus inverse temperature for the 2nm $Ge_{0.945}Sn_{0.055}$ QDs in the (a) high-temperature range and (b) low temperature range. Solid lines are single activation energy fits to data.

Arrhenius plots of the slow decay times are presented in Fig. 3.6 together which are fitted using following equation where, C_1 and C_2 are constants, and E_A is an activation energy,

$$\tau(T) = \frac{C_1}{1 + C_2 e^{-E_A/kT}} \ldots\ldots\ldots (4)$$

The activation energies obtained from the fits are E_A = 20±1 meV for the low temperature range and E_A = 157±31 meV for the high temperature range.

Table 3: *Extracted Activation Energy from Integrated PL Intensity for Different Size and Composition of GeSn Quantum Dots*

~2nm				**~4nm**			
5.5%		**6.6%**		**2.4%**		**5.9%**	
E_{A1} (meV)	**E_{A2} (meV)**	**E_{A1} (meV)**	**E_{A2} (meV)**	**E_{A1} (meV)**	**E_{A2} (meV)**	**E_{A1} (meV)**	**E_{A2} (meV)**
25±4	133±28	27±7.3	127±16	19±2	185±32	17±3	52±7

Note that these values are comparable to E_{A1} and E_{A2}, respectively, obtained from the fits to integrated PL as indicated in Table 3. GeSn ultrasmall QDs discussed here show unique properties in terms of their change in PL position to shorter wavelengths with increasing temperature. Using steady-state PL and TRPL data and considering possible changes in energy gap, carrier population in different states within QD with temperature, a clear understanding of the carrier dynamics can be gained. The possible reasons for the difference in behavior between the two sizes of QD's is further explained in the next section in this chapter by the formulation of a theoretical model.

3.2 Theoretical Model

To better understand the overall temperature dependent behavior observed in the previous section, a rate equation model will be introduced in this section. This model considers the change in carrier

distributions across the bright and dark excitonic states and trap states to elucidate the behavior shown by the quantum dots. Both sizes of quantum dots exhibit change in integrated PL intensity with temperature. To account for the distribution of carriers between different states, longitudinal optical phonons are interacting with the carriers, resulting in phonon absorption and emission processes

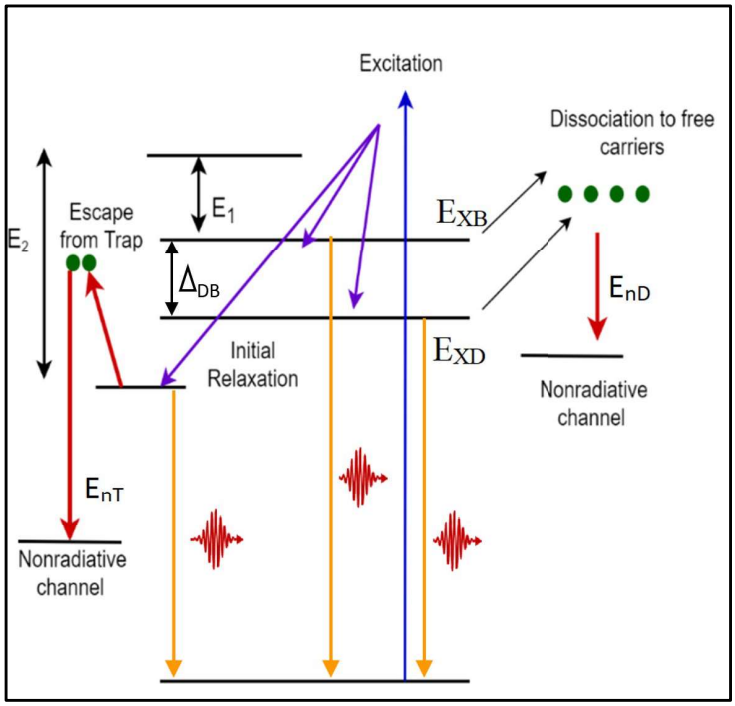

Figure 3.7: Relaxation and carrier distribution in a GeSn alloy quantum dot showing radiative and non-radiative recombination pathways after optical excitation. Purple lines show initial relaxation post excitation. Orange Lines indicated radiative transitions and red lines show non-radiative transitions. E_{nD} and E_{nT} indicate the energies for the activation of the non-radiative pathways.

In this model, an energy level structure as shown in figure 3.1 is considered. It consists of ground state dark exciton and bright exciton states with radiative decay rates κ_b and κ_d, respectively. The energy splitting Δ_{DB} between these two states depends on the system of QD being investigated. To transfer from the bright and dark exciton levels to the surface trap states, the carriers must overcome the barrier, denoted by E_1 by absorbing longitudinal optical phonons (LO) and then emit phonons to reach the trap state at energy E_2 with respect to the barrier level. The reverse process occurs via first absorption of phonon to overcome barrier E_2 and then emission of phonons with energy E_1 for the reverse process to occur.

The excitation source is a laser with pulse width is ~150 fs and with 12.5ns time-period that can be extended up to milliseconds using a pulse picker. This allows enough time for the initially excited carriers to relax to the dark, bright and trap states. This initial relaxation takes place in the order of pico-second and the redistribution of carrier population that follows hence has been regarded to have no dependence on the initial excitation in this model. At low temperatures, the dark excitons with long lifetime predominantly take part in the emission process along with the carriers that are in the surface trap states with slow decay time (μs range). Due to carriers having low thermal energy, the non-radiative recombination and hence change in integrated PL intensity with change in temperature is low in this regime. As temperature increases, carriers with thermal energy $E_1 < k_B T < E_2$ have greater probability of overcoming the barrier. More carriers can populate the surface states from bright and dark states and various non-radiative channels are activated. So, the integrated PL intensity starts to drop. At the same time, carriers with high thermal energy can repopulate the high energy bright states and dark states from trap states. Bright excitons at higher temperature then start to dominate the emission process as they have higher probability of recombination and faster decay time. The initial value of bright and dark exciton ground state is set equal to the value at 15K. With change in temperature there is change in the levels that is accounted for in the model using Varshni's empirical formula,

$$E_g(T) = E_{g0} - \frac{\alpha T^2}{\beta + T} \quad \ldots\ldots\ldots (5)$$

where α and β are fitting parameters and β relates to Debye temperature of a given semiconductor material and fitted to the experimental data. This change in bright and dark exciton levels coupled with the change in carriers in each state can result in a shift of the emission energy to higher or lower energy when temperature changes from low to high. This behavior manifests itself in the photoluminescence spectra as either blue shift or red shift in the peak emission energy. The change in carrier population of each state is considered by defining relaxation rates κ_{B-T} and κ_{D-T}. The

relaxation rates for the carriers from the bright (κ_{B-T}) and dark (κ_{D-T}) states involve first absorption of phonons to overcome the barrier given by E_1 (from bright exciton level) or $E_1+\Delta_{DB}$ (from dark exciton level) and then subsequent emission of phonons as the carriers relax to the trap state. The corresponding rates can be written as,

$$\kappa_{B-T} = k_0(\exp\left(\frac{E_{ph}}{K_BT}\right)-1)^{\frac{-E_1}{E_{ph}}} \times \left(\frac{\exp\left(\frac{E_{ph}}{K_BT}\right)}{\exp\left(\frac{E_{ph}}{K_BT}\right)-1}\right)^{\frac{E_2}{E_{ph}}} \ldots\ldots(6)$$

$$\text{and, } \kappa_{D-T} = k_0(\exp\left(\frac{E_{ph}}{K_BT}\right)-1)^{\frac{-(E_1+\Delta_{DB})}{E_{ph}}} \times \left(\frac{\exp\left(\frac{E_{ph}}{K_BT}\right)}{\exp\left(\frac{E_{ph}}{K_BT}\right)-1}\right)^{\frac{E_2}{E_{ph}}} \ldots\ldots(7)$$

where k_o is a universal rate constant, which characterizes the efficiency of the thermally induced radiative relaxation processes.

Here, $(\exp(E_{ph}/(k_BT))-1)^{-n}$ is the probability for a carrier to absorb n phonons of energy E_{ph}. Also, $[(\exp(E_{ph}/(k_BT)))/((\exp(E_{ph}/(k_BT))-1))]^m$ is the probability for a carrier to emit m phonons of energy E_{ph}. The number of phonons (N_p) with energy equal to E_{ph} is given by Bose–Einstein statistics. Carriers can repopulate the bright (κ_{T-B}) and dark (κ_{T-D}) states from the trap states with sufficient energy as the temperature rises. These rates are given by,

$$\kappa_{T-B} = k_0(\exp\left(\frac{E_{ph}}{k_BT}\right)-1)^{\frac{-E_2}{E_{ph}}} \times \left(\frac{\exp\left(\frac{E_{ph}}{k_BT}\right)}{\exp\left(\frac{E_{ph}}{K_BT}\right)-1}\right)^{\frac{E_1}{E_{ph}}} \ldots\ldots(8)$$

$$\text{and, } \kappa_{T-D} = k_0(\exp\left(\frac{E_{ph}}{k_BT}\right)-1)^{\frac{-E_1}{E_{ph}}} \times \left(\frac{\exp\left(\frac{E_{ph}}{k_BT}\right)}{\exp\left(\frac{E_{ph}}{K_BT}\right)-1}\right)^{\frac{E_1+\Delta_{DB}}{E_{ph}}} \ldots\ldots(9)$$

The carriers with sufficient energy also redistribute between bright and dark excitonic states which is given by the following equations,

$$\kappa_{D-B} = k_0(\exp\left(\frac{E_{ph}}{k_BT}\right)-1)^{\frac{-\Delta_{DB}}{E_{ph}}} \ldots\ldots(10)$$

$$\kappa_{B-D} = k_0\left(\frac{\exp\left(\frac{E_{ph}}{K_B T}\right)}{\exp\left(\frac{E_{ph}}{k_B T}\right) - 1}\right)^{\frac{\Delta_{DB}}{E_{ph}}} \ldots\ldots (11)$$

As the temperature changes, these transition rates change slightly as Δ_{DB} has some temperature dependence.

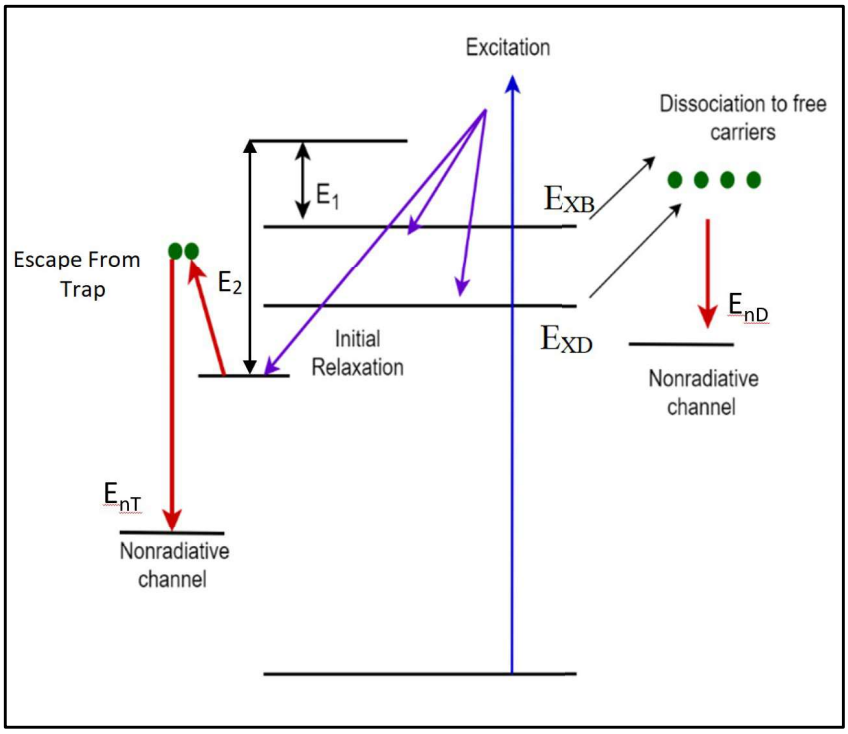

Figure 3.8: Non-radiative recombination pathways after optical excitation. Purple lines show initial relaxation post excitation and red lines show non-radiative transitions. E_{nD} and E_{nT} indicate the energies for the activation of the non-radiative pathways.

As shown in Figure 3.8, To account for the change in integrated PL intensity from non-radiative transitions, two nonradiative recombination channels are introduced into this model. One of the channels accounts for non-radiative transition from the surface trap states. Excitons with sufficient thermal energy (E_{esc}), first escape the trap and then non-radiatively recombine through emission of phonons via the channel denoted with energy (E_{nT}). Excitons can also dissociate with temperature and become free carriers (electron-holes). Excitons with energy E_{dis} which can be compared to their binding energy can dissociate to form free carriers which can later non radiatively recombine with via channel with energy denoted by E_{nD}. As the system in consideration

is a highly quantum confined structure, the free carrier radiative recombination is insignificant in comparison to the exciton recombination. It has been observed in certain thin film QD systems like perovskites, if the excitation density is sufficiently high that there can be significant number of free carriers as well as excitons formed in the system [66]. However, for the low range of excitations employed experimentally, has not been taken into consideration and only radiative recombination from the excitons are considered in this model as the effect would not be significant.

First, the rate of the nonradiative transition that is associated with the escape from the trap is given by

$$\kappa_{esc} = k_0(\exp\left(\frac{E_{ph}}{k_B T}\right) - 1)^{\frac{-E_{esc}}{E_{ph}}}(\frac{\exp\left(\frac{E_{ph}}{k_B T}\right)}{\exp\left(\frac{E_{ph}}{k_B T}\right) - 1})^{\frac{E_{nT}}{E_{ph}}} \ldots\ldots\ldots (12)$$

To recombine non-radiatively, the carriers must first escape the trap, which requires energy E_{esc}, and then emit phonons with energy $E_{nT.}$ The non-radiative recombination rate associated with the exciton dissociation is

$$\kappa_{dis} = k_0(\exp\left(\frac{E_{ph}}{k_B T}\right) - 1)^{\frac{-E_{dis}}{E_{ph}}}(\frac{\exp\left(\frac{E_{ph}}{k_B T}\right)}{\exp\left(\frac{E_{ph}}{k_B T}\right) - 1})^{\frac{E_{nD}}{E_{ph}}} \ldots\ldots (13)$$

κ_{dis} and κ_{esc}, together account for the non-radiative processes that occur in the QD system with change in temperature and directly affect the onset of decrease in integrated PL intensity or the PL quenching.

The following rate equations then govern, the change in bright and dark state populations,

$$\frac{dn_{bright}}{dt} = -(\kappa_b + \kappa_{B-T} + \kappa_{B-D} + \kappa_{dis})n_{bright} + \kappa_{T-B}n_{trap} + \kappa_{D-B}n_{dark} \ldots. (14)$$

$$\frac{dn_{dark}}{dt} = -(\kappa_d + \kappa_{D-T} + \kappa_{D-B} + +\kappa_{dis})n_{dark} + \kappa_{T-D}n_{trap} + \kappa_{B-D}n_{bright} \ldots. (15)$$

$$\frac{dn_{trap}}{dt} = -(\kappa_{Trap} + \kappa_{T-D} + \kappa_{T-B} + +\kappa_{esc})n_{trap} + \kappa_{D-T}n_{dark} + \kappa_{B-T}n_{bright} \ldots . (16)$$

Here, n_{bright}, n_{dark}, and n_{trap} are the carrier populations of the bright, dark, and trap states, which are time and temperature dependent, and κ_b , κ_d, κ_{trap} are, respectively, the radiative relaxation rates of carriers from the bright, dark, and trap states. The relaxation times for the dark exciton and trap states are in the order of microseconds while that for bright excitons is in nanoseconds. An initial population is assigned to the trap state post excitation. The remaining population is set to be $N(t = 0) = n_{bright} + n_{dark}$, while the population of the bright and dark states at t = 0 is assumed to follow the Boltzmann distribution $(n_{bright}/n_{dark}) = e^{(-\Delta E)/(k_B T)}$.

As mentioned earlier in section 3.1, the carriers can relax fast within ps after excitation and taking into the account the excitation pulse (~150 fs), this initially excited carriers are not affected by the source after excitation. Taking the redistribution of carriers with change in temperature and normalizing to initial carrier distribution, integrated PL intensity is then described by the change in exciton population due to radiative decay from bright, dark states and the trap states

$$\frac{dn_{radiative}}{dt} = \kappa_B n_{bright} + \kappa_D n_{dark} + \kappa_{trap} n_{trap} \ldots . (17)$$

To model the peak position, the change in carriers that radiatively recombine is considered for each temperature from the three states: bright exciton, dark exciton, and trap state. Radiative recombination from each state is assume to produce a Gaussian shaped spectrum with finite linewidth (equal to the linewidth data obtained from experiment) and the maximum intensity of each spectrum is considered proportional to the number of carriers taking part in radiative recombination in that state at that temperature. The sum of these Gaussian shaped radiative spectra gives the overall radiative recombination spectrum at a temperature. The position of the peak emission for each temperature can be determined from this resultant spectrum. Details of the application of this model and the resultant fitted parameters will be discussed in Section 3.3.

3.3 Results and Discussion: Extracted Parameters from Rate Equation Modelling of Carrier Dynamics with Change in Temperature and Composition of QD and Comparison with Experimental Observations

In this section, the model developed in section 3.2 has been applied to simulate change in PL peak position, carrier density in different states and integrated Pl intensity and compared with the experimental data observed and detailed in section 3.1. Here, phonon energy E_{ph} has been set equal to E_{ph} = 30.6 meV [67] which is the Longitudinal optical (LO) phonon energy observed in bulk Ge. Alloying has shown to decrease the energy of LO phonons [68] in different QD systems like GaInAs on InP substrate. Within the composition range of interest (5.5% to 6.6%), there should be little change (0.05 meV) in their energy. The transition rates for dark and bright exciton states were also fixed at values obtained from experiments. For 2nm QDs, Δ_{DB} is set to bet 25 meV [32] as estimated for ~2nm sized quantum dots at 15K. To account for the changing energy gaps with temperature, Varshni's empirical formula was used to induce a variation in the level of bright and dark exciton state with temperature given by,

$$E_g(T) = E_{g0} - \frac{\alpha T^2}{\beta + T}.$$

The β parameter in Varshni's empirical formula is regarded as the Debye temperature of the material. Although, alloy composition changes Debye temperatures, but the percent variation in Sn in the samples (less than 5K with 5% Cu inclusion in Ni)[69] under consideration is low and hence kept equal to the value of bulk Ge. Parameters α for bright exciton (α_b) and dark exciton (α_d) were derived from fit to the model. The temperature dependences of surface trap states and non-radiative channel energy levels were not considered in these fits although are likely to have some dependence on temperature.

To implement the model to account for the observed behavior of the QD systems under consideration uniqueness plots were utilized to set the value of certain parameters in the model.

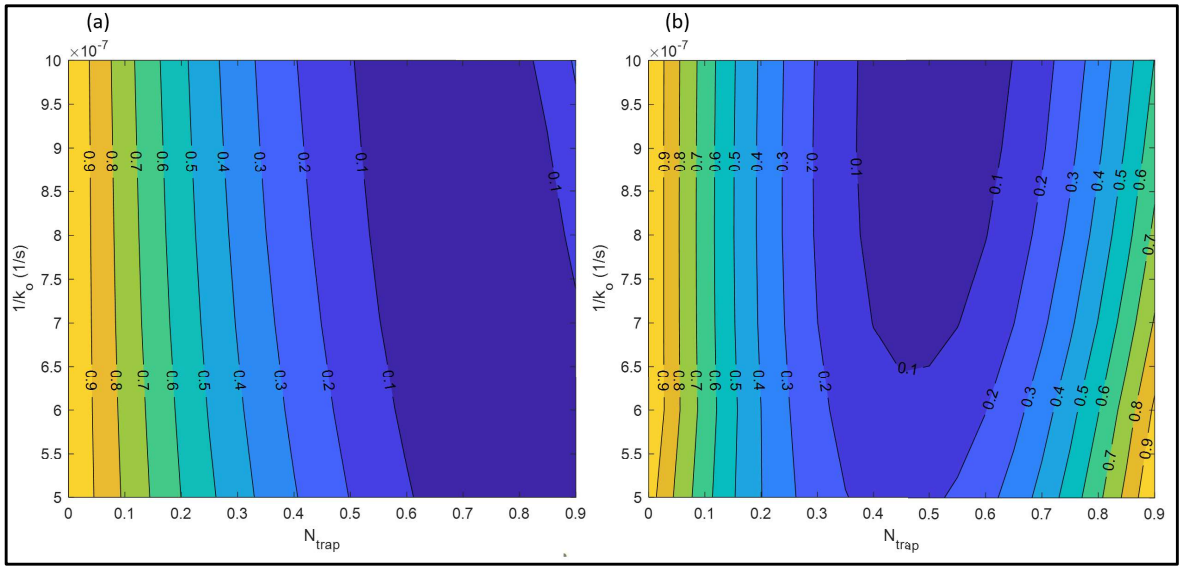

Figure 3.9: Uniqueness plots for change in mean square error in the fits of (a) Integrated PL Intensity and (b) PL peak position as a function of the initial trap concentration for ultra-small (~2nm) $Ge_{1-x}Sn_x$ with 5.5% Sn.

The uniqueness plots were used to determine the optimal concentration of trap and thermalized carrier transfer rate k_o in this QD system to get best fit for the experimental data. The error estimations were performed for larger range of values of k_o and n_{trap} first and then multiple iterations were used to get the optimal value in a much narrower range. The uniqueness plots for the 2nm QD with 5.5% is shown in figure 3.11. As can be seen from 3.11(a), more than 50% trap concentration regardless of the value of k_o gives 20% (or less) mean square error (MSE) in the fits for integrated PL intensity. At the same time, trap concentration of 50% (b) gives 10% for less value of MSE for the fits to PL peak position for k_o values more than $\frac{1}{6.5\times10^{-7}}\ s^{-1}$. A value of 65% for initial population of carriers in trap and a value of $k_o = \frac{1}{6=8\times10^{-7}}\ s^{-1}$ was set in this model for 5.5% Sn and 75% was set for 6.6% Sn (Appendix A1), to keep the overall MSE of fit within reasonable limits of 15% (or less) error percentile. The value of k_0 represents the overall efficiency of the carrier transfer process in the quantum dot system and the value was set to be in the order of ~10^6 s^{-1} and was determined via uniqueness plot analysis for the overall fit. These values are comparable to values obtained for PbS quantum dot systems with comparable size distribution [57].

Change in composition of Sn is also estimated to have an effect of lowering of exciton splitting. However, in this model that change with composition within a specific size range was not considered as the composition does not vary significantly.

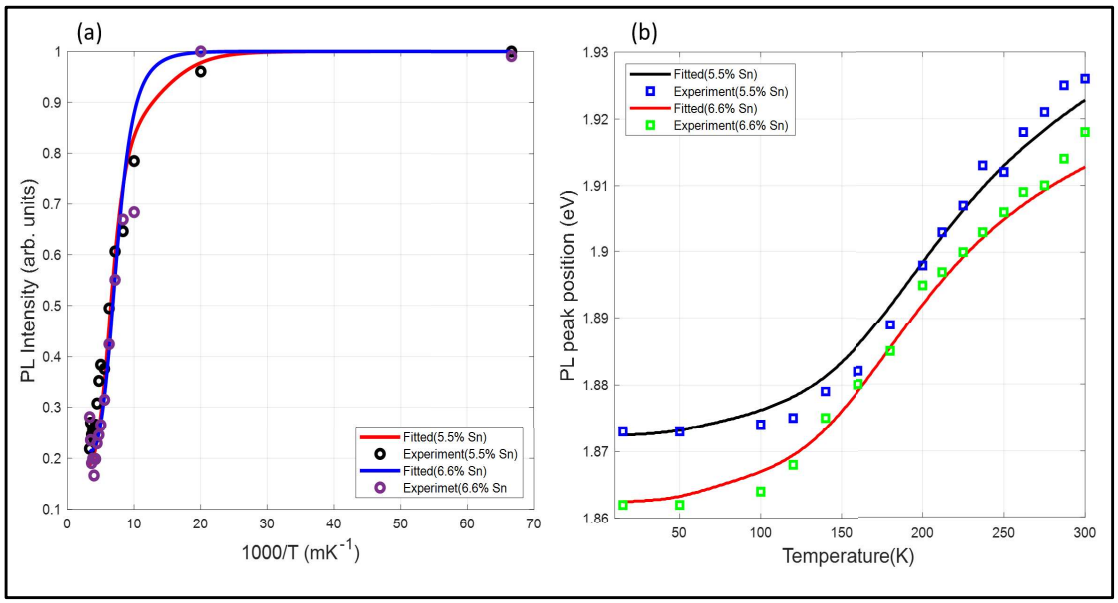

Figure 3.10: Ultrasmall QD of size ~2nm (a) Experimental Integrated PL Intensity of $Ge_{1-x}Sn_x$ alloy QD plotted as a function of temperature (dotted lines) with fits derived from the model(solid lines) for 5.5% (red line and black dots) and 6.6% Sn composition (blue line and violet dots) (b) (a) Experimental change in PL peak position of $Ge_{1-x}Sn_x$ alloy QD is plotted as a function of temperature (dotted lines) with fits derived from the model(solid lines) for 5.5% Sn (black line and blue square box) and 6.6% Sn (red line and green square box)

Figure 3.9 shows the fits for integrated PL intensity and PL peak position plotted alongside the experimental data. The integrated PL was obtained by taking the sum of radiative decay from bright, dark excitons and trap states (time interval of about 10^{-10} ns) for the total range of time of the simulation at each temperature. The relative radiative intensity for each of the three states that is dark, bright and trap state was first estimated. Then a gaussian profile of PL spectrum was obtained with fixed linewidth with intensity set equal to relative radiative intensity. The sum of the three gaussian spectrum gave the overall PL spectrum at that temperature. Peak emission energy was determined from taking sum of the resultant Gaussian spectra. The results obtained showed root mean square error (RMSE) of 0.084 (6.6% Sn) and 0.092 (5.5% Sn) for the fits to integrated PL intensity data obtained from experiments. For peak PL fits, they show RMSE values of 0.013 and 0.016 for 5.5% and 6.6% Sn, respectively. The confidence bounds change the fit

within 10% goodness of data for both set of fits. Table 4 gives the fitted parameters along with the set parameters for the ultra-small $Ge_{1-x}Sn_x$ QD for both compositions.

Table 4: *Fitted and Fixed Parameter (~2nm) $Ge_{1-x}Sn_x$ Carrier Dynamic Model*

Sn Content	**Fixed Parameters**					
	E_{ph}	**$\kappa_b(s^{-1})$**	**$\kappa_d(s^{-1})$**	**$k_o(s^{-1})$**		**β(K)**
	30.6	$\frac{1}{12\times10^{-9}}$	$\frac{1}{24\times10^{-6}}$	$\frac{1}{8.5\times10^{-7}}$		290
Sn Content	**Fitted Parameters**					
5.5%	**E_1(meV)**	**E_2(meV)**	**E_{dis}(meV)**	**E_{nD} (meV)**	**E_{esc}(meV)**	**E_{nT} (meV)**
	60.18±9.5	105.2±10.3	25.25 ± 1.52	40.3 ±2.3	62.3±13.8	125.12 ±5.6
	α_d(meV/K)			**α_b(meV)/K**		
	0.18±0.012			0.092±0.0029		
6.6%	**E_1(meV)**	**E_2(meV)**	**E_{dis}(meV)**	**E_{nD} (meV)**	**E_{esc}(meV)**	**E_{nT} (meV)**
	58.18±10.6	110.8±9.2	33.12 ±3.8	35.12 ±8.1	55.3±4.6	120.12 ±20.8
	α_d(meV/K)			**α_b(meV)/K**		
	0.17±0.031			0.090±0.0076		

E_1 represents a barrier that the carriers need to overcome to redistribute themselves between different energy levels within the QD and show little dependence on the Sn composition. This is related to the confinement effect of the dots and hence has a more size dependent behavior as will become clear in the discussions later in this chapter. E_2 is defined relative to the barrier E_1 and represents shallow trap states on the surface that take part in the radiative recombination with long lifetime in the μs range and it has been kept equal to the radiative transition rate of dark exciton for sake of simplicity in this model. Taking into account, Δ_{DB} and the energy level E_2 with respect to barrier E_1, the radiative recombination from the trap states can account for the additional 10 to 20 meV shift observed in the PL peak position from the predicted values [32]. E_{dis} and E_{nD}

associated with the possible exciton dissociation energy of exciton and the subsequent loss of those carriers to non-radiative recombination channels. E_{nT} are non-radiative recombination channel through which carriers escaping the surface trap with thermal energy are lost and it is consistent with the activation energies derived from the experimental data. E_{sc} represent the energy required for the trapped exciton from surface states to escape and its shows a decrease with increasing Sn content. As have been discussed before, increasing Sn content could make more non-radiative recombination channels available by introducing defects into the system which could lead to this lowering of energy. The α values reported in other nanocrystal systems like CdTe for around ~3nm nanocrystal is around 0.473 meV/K and 0.519 meV/K [70] and for colloidal CdSe/ZnS core-shell structures is around 0.41 meV/K [71] for ~2nm QD size. Fitted values obtained here are significantly lower but can be deemed reasonable given the variation of the QD along with change in composition.

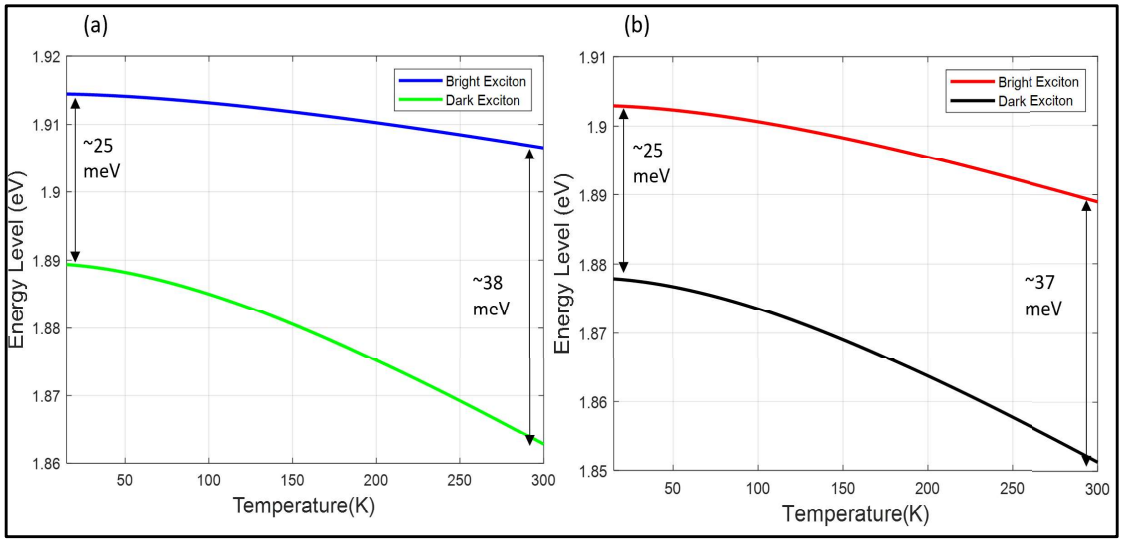

Figure 3.11: Change in Bright and Dark Excitonic Energy Levels with Temperature for 2nm $Ge_{1-x}Sn_x$ QD with (a) 5.5% Sn (b) 6.6% Sn

The change of PL peak position and the observed change in lifetime of the experimental data for the 2nm dots, can be understood further by taking a look at the change in excitonic levels with change in temperature and the total population changes in certain time intervals after excitation which can be extracted from the theoretical model. As can be seen in Figure 3.11, the bright and

dark exciton decrease with temperature, but the bright exciton level is still at higher energy at 300K compared to the dark exciton level at 15K. Also, there is gradual lowering of the excitonic levels, and this can account for the observed increase in PL peak emission in the experimental data. The PL peaks however do not change significantly in the 15K to 300K region. To better understand decay dynamics due to carrier transfer, the change in carrier population taking part in different states can be extracted from the theoretical model. The radiative decay intensities in different energy states can be extracted from total radiative intensity. At any given temperature and at any given time,

$$n_{radiative}(t,T) = \kappa_b n_{bright}(t,T)\Delta t + \kappa_d n_{dark}(t,T)\Delta t + \kappa_{trap} n_{trap}(t,T)\Delta t.$$

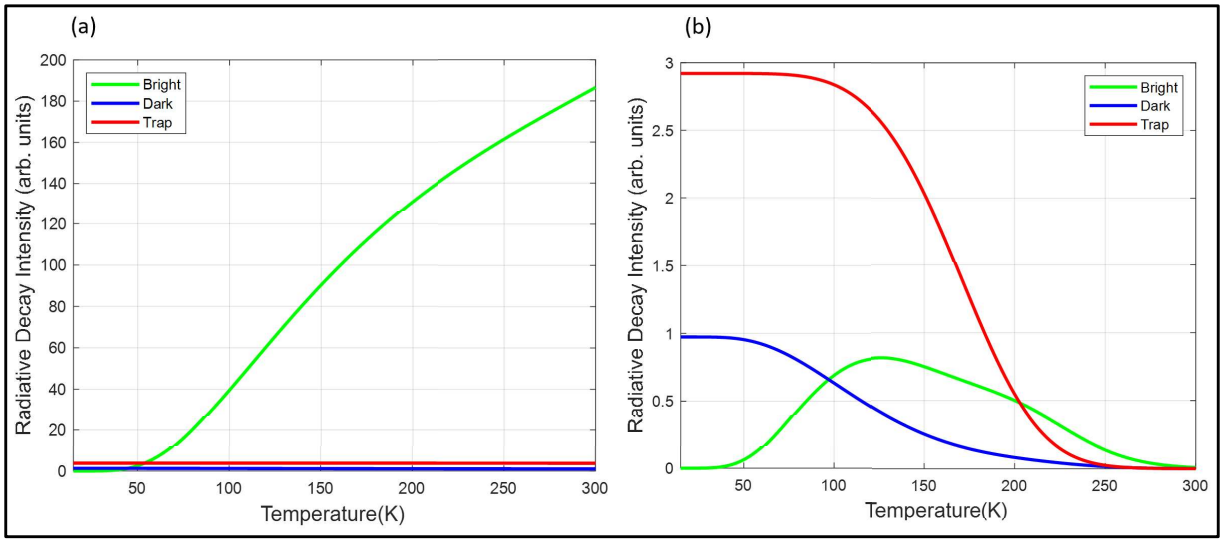

Figure 3.12: (a) Population of Carriers in Bright, Dark and Trap States that are lost via radiative recombination at (a) t = 10ns and (b) t= 5μs after excitation for ~2nm QD with 6.6% Sn.

As can be seen from Figure 3.12 (a), 10ns after excitation, the radiative decay is dominated by radiative recombination from the bright exciton state. Beyond temperature of 50K, over the entire range of temperatures, bright excitons contribute more and more. That is because bright state radiative transition rate is in the order of few ns, so the population lost from bright state for radiative recombination is fast and this is apparent in the Figure 3.12(a). There is still many carriers in trap and dark states in the lower temperature regime, but they have μs lifetime and hence cannot radiatively recombine fast and contribute little at t=10ns time. With time, carriers can redistribute

themselves in these 3 states and some carriers non-radiatively recombine with activation of various channels. At t = 5μs, beyond 50K, bright exciton recombination starts to emerge. There is, however, a large portion of radiative recombination happening via dark and trap states. With increase in temperature, more and more of these dark and trap state excitons are redistributed to either bright states or lost via non-radiative recombination. Beyond 50K, the radiative recombination from dark state starts to decrease and beyond 250K there is no radiative recombination happening via dark states. For the trap state population, beyond 100K there is sharp decrease in radiative recombination. Beyond ~200K, entirely bright state population dominates the radiative recombination. So, between 100K to 200K, there is redistribution of carriers in between bright, dark and trap states with temperature. So, PL decay time would be dominated by the state that contributes most to recombination in this temperature range while the PL peak position will show a gradual shift. Comparing this to the decay times observed from experimental TRPL measurement in section 3.1, it is evident that the shift to ns lifetime beyond 200K from μs is in line with the change in the radiative recombination intensities observed here.

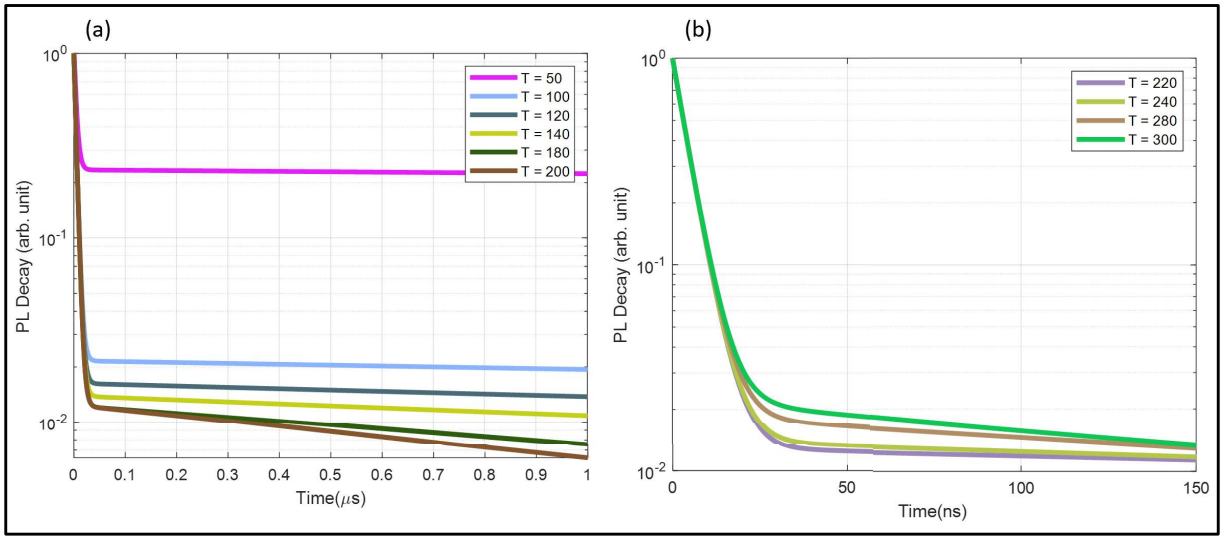

Figure 3.13: Normalized PL decay curves obtained from the modelling for different temperature ranges

To further investigate the change in decay time relation with the change in carrier population, PL decay was simulated for different temperatures (Figure 3.13). As can be seen, more than two

orders of magnitude decays are observed for the temperatures above 220K in the ns regime. At the same time, for temperatures lower than 200K, most of the PL decay occurs in the μs regime.

So, looking at 10ns and 5μs time window after excitation, it is evident that interplay between dark, bright and trap state population with temperature shift the PL peak position gradually towards higher energy going from 15K to 300K and it also results in a drastic change in PL decay time with bright excitons with ns lifetime being completely responsible for radiative decay after 200K temperature. The results obtained from the model match the experimental observation in section 3.1 with good accuracy. Quantum Yield was also calculated from this model by considering, the radiative to non-radiative transitions occurring at any given temperature. For, the 2nm samples quantum yields are found to be around 21% and 23% for 5.5% and 6.6% Sn composition, respectively. The model considers only two pathways for non-radiative recombination when there are possibly many more channels that are activated in ultra-small quantum dots. This could be probable reason of the overestimation in the value of Quantum Yield.

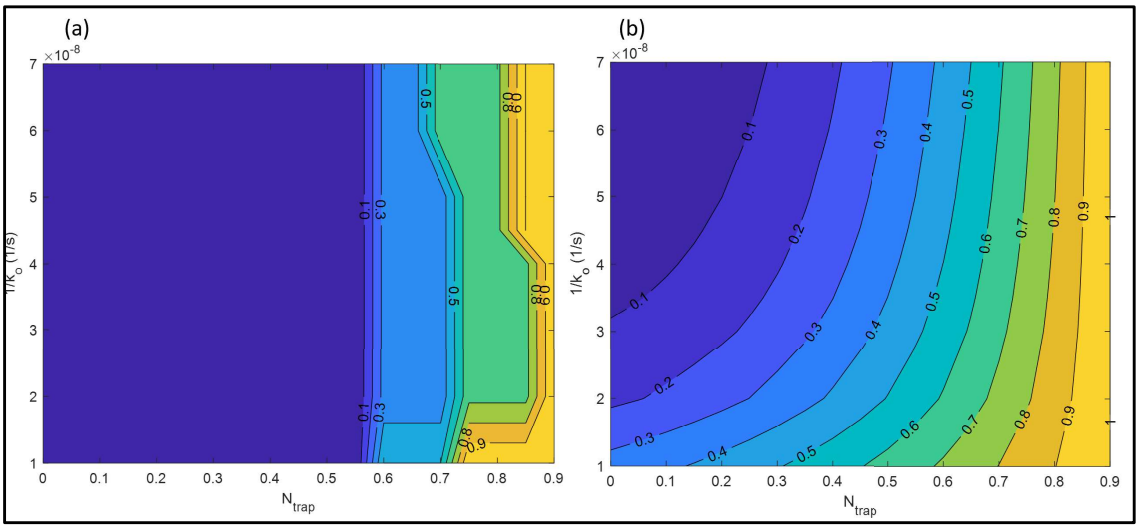

Figure 3.14: Uniqueness plots for change in mean square error in the fits of (a) Integrated PL Intensity and (b) PL peak position as a function of the initial trap concentration for larger (~4nm) $Ge_{1-x}Sn_x$ with 2.4% Sn.

For larger QDs, initial carrier concentrations (N_{trap}) and k_o were again set by considering the uniqueness plots for MSE of the two fits. Initial trap carrier concentration was set to 10% (2.4%

Sn) and 15% (5.9% Sn). As can be seen from Figure 3.14, the value of MSE for integrated PL intensity fit shows little dependence on k_o for trap concentration up to 55% with the MSE value being below 10% for concentrations up to 55%. For the PL peak fit, $1/k_o$ values of $\frac{1}{3.3\times10^{-8}}\ s^{-1}$ and larger, with trap concentrations of 25% or less gives MSE less than 20%. Again, $\frac{1}{k_o} = \frac{1}{3.3\times10^{-8}}\ s^{-1}$ and trap concentration of 10% was chosen to keep the value of MSE below 15% or less for the ~4nm QDs with 2.4% Sn. The 4nm QDs are easier to passivate owing to their greater surface to volume ratio with organic ligands hence this lower concentration of surface traps and lower value of initial carrier population in these QDs are within reasonable limits of theoretical expectations.

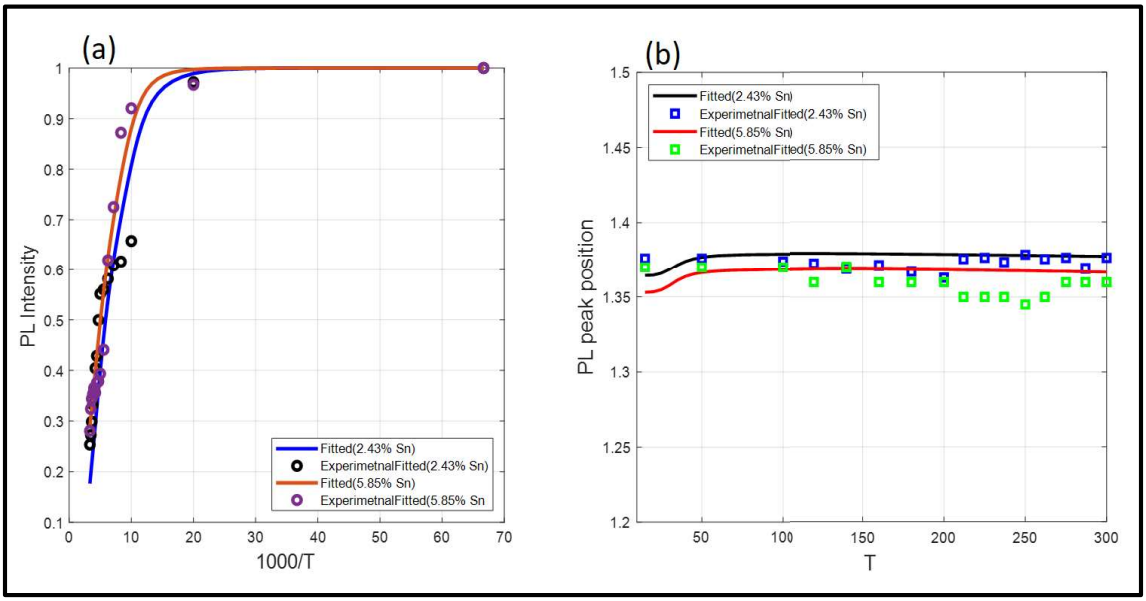

Figure 3.15: QD of size ~4nm (a) Experimental Integrated PL Intensity of $Ge_{1-x}Sn_x$ alloy QD plotted as a function of temperature (dotted lines) with fits derived from the model(solid lines) for 2.4% (blue line and black dots) and 5.9% Sn composition (orange line and violet dots) (b) (a) Experimental change in PL peak position of $Ge_{1-x}Sn_x$ alloy QD is plotted as a function of temperature (dotted lines) with fits derived from the model(solid lines) for 2.4% Sn (black line and blue square box) and 5.9% Sn (red line and green square box)

Figure 3.15 represents the experimental data along with the fit from model for the ~4nm QDs. The obtained fits showed root mean square error (RMSE) of 0.05 (2.4% Sn) and 0.14 (5.9% Sn) for the fits to integrated PL intensity data obtained from experiments. For peak PL fits, RMSE values of 0.007 and 0.015 for 2.4% and 5.9% Sn, respectively, were obtained. The confidence bounds

change the fit within 10% goodness of data for both set of fits.

Table 5: *Fitted and Fixed Parameter (~4nm) $Ge_{1-x}Sn_x$ Carrier Dynamic Model*

Sn Content	**Fixed Parameters**					
	E_{ph}	**$\kappa_b(s^{-1})$**	**$\kappa_d(s^{-1})$**	**$k_o(s^{-1})$**		**β(K)**
	30.6	$\frac{1}{30\times10^{-9}}$	$\frac{1}{11\times10^{-6}}$	$\frac{1}{3.3\times10^{-8}}$		290
Sn Content	**Fitted Parameters**					
2.43%	**E_1(meV)**	**E_2(meV)**	**E_{dis}(meV)**	**E_{nD}(meV)**	**E_{esc}(meV)**	**E_{nT} (meV)**
	47.58±16.2	125±12.6	35.8±2.1	20.6 ±4.7	50.1±2.5	160.12 ±13.1
	α_d(meV/K)			**α_b(meV)/K**		
	0.01±0.015			0.031±0.0015		
5.86%	**E_1(meV)**	**E_2(meV)**	**E_{dis}(meV)**	**E_{nD}(meV)**	**E_{esc}(meV)**	**E_{nT} (meV)**
	44.58±10.9	95.58±12.4	33.1±1.03	21.3 ±5.9	49.01±0.9	70.12 ±5.6
	α_d(meV/K)			**α_b(meV)/K**		
	0.013±0.011			0.04±0.003		

As can be seen from the Table 5, the barrier value E_1 again shows lowering with increase of Sn and it is noticeable here that barrier height is larger for 2nm dots compared to 4nm dots. This is possibly due to quantum confinement being stronger in smaller dots. The initial carrier population being low in the trap states, the contribution from these state in lower temperature end is not significant. The significant lowering of the value of non-radiative channel energy with Sn concentration going from 2.4% to 5.9% is indicative of more core non-radiative channels being available with change in size. At the same time E_2 values are higher when compared to activation energy and exciton splitting indicating deep level defects. Dissociation values obtained from the

fit however are comparable to the smaller sized counterparts. The size dispersion and alloying effect could together account for this increase in binding energy. Two non-radiative channels were considered in this fitting from the dissociation of carriers and the surface trap states denoted by energy E_{nT} and E_{nD}, and they were obtained from the fit. When compared to activation energies obtained from the experimental data, the values of energy levels for non-radiative channels are within similar range.

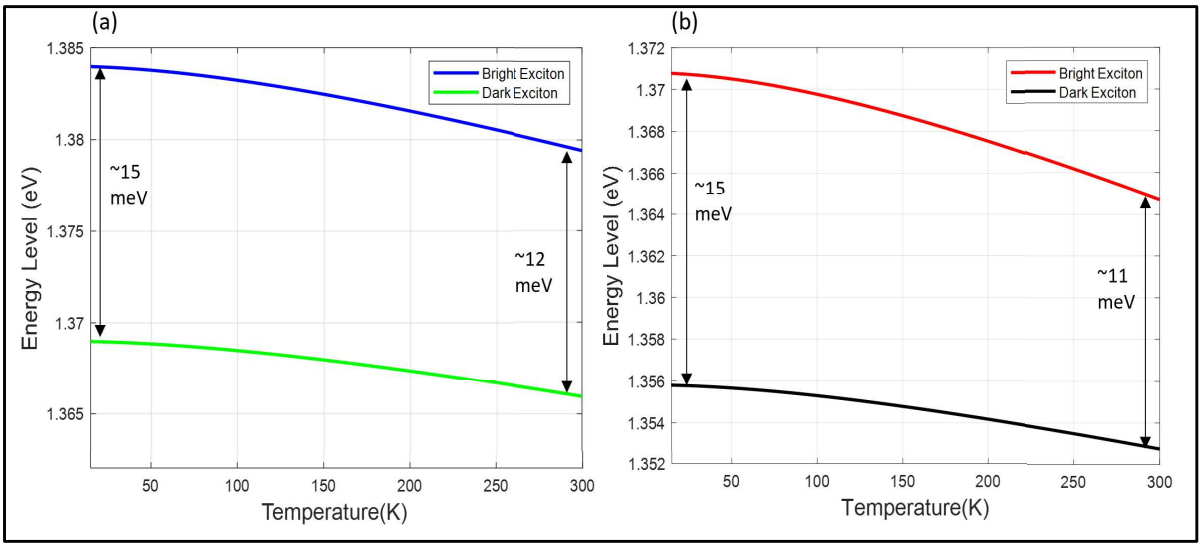

Figure 3.16: Change in Bright and Dark Excitonic Energy Levels with Temperature for 4nm $Ge_{1-x}Sn_x$ QD (a) for 2.4% Sn (b) 5.9% Sn

For, 4nm QDs, the value of exciton splitting is set to be 15 meV at 15K. This is consistent with the fact that larger size QD have lower values of exciton splitting [72, 73] and change in exciton level is shown in Figure 3.15. Varshni's empirical formula was used and the β parameter in Varshni's empirical formula is again set equal to Debye temperature of the material that is Ge. Parameters α for bright exciton (α_b) and dark exciton (α_d) were derived from fit to the model. As can be seen there is gradual lowering of excitonic levels and exciton splitting with temperature but compared to the 2nm system, the change is much smaller. So, even when the bright excitons are activated their energy level is comparable to the dark level before lowering of energy gap. Hence, there should be little to no observed shift as was discussed in the experimental results in section 3.1.

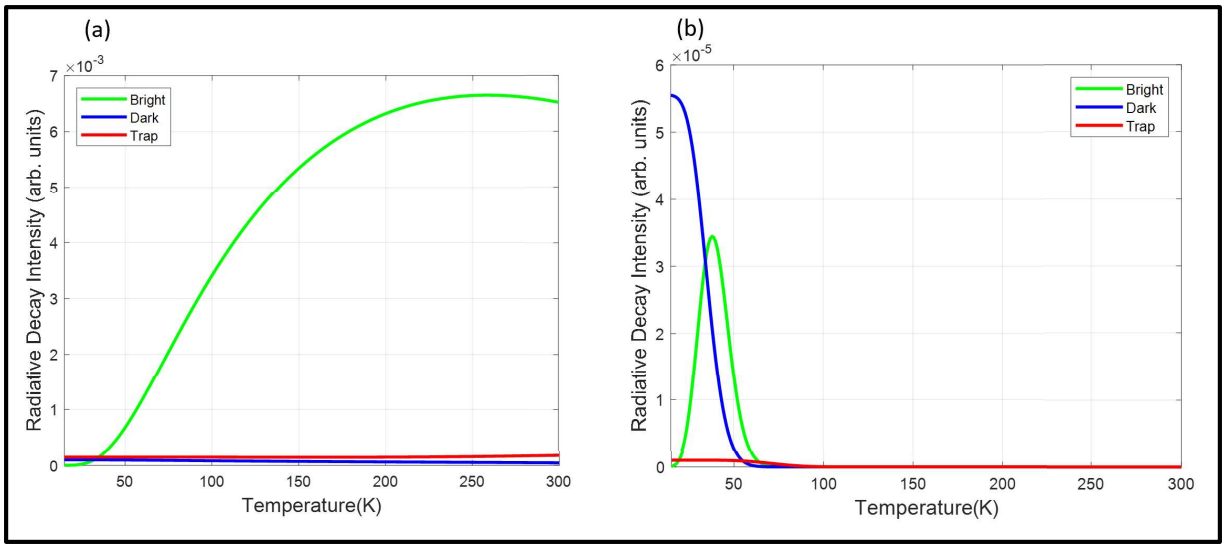

Figure 3.17: (a) Population of Carriers in Bright, Dark and Trap States that are lost via radiative recombination at (a) t = 10ns and (b) t= 5µs after excitation for ~4nm Size QD with 5.9% Sn.

Figure 3.17 gives the change in population undergoing radiative recombination with change in time between the bright, dark and trap states for 4nm QD with 2.4% Sn. As is evident, right after excitation, there is number of carriers in dark state and trap state but exceptionally low population of carriers in bright state at 15K. But the bright excitons have lifetime of ns so the in time window of t=10ns after excitation the bright states dominate after 30K temperature. Since, the trap state energetically represents a deep level trap, carriers do not repopulate bright or dark state that easily. Instead, the non-radiative recombination channels get activated with temperature and most likely causes the sharp decrease post 50K via dissociation of excitons first and then from the trap states. As majority of radiative recombination happen via excitonic states and there is smaller change in exciton splitting energy which changes in temperature, the peak emission from PL does not show significant change with change in temperature. At t=5µs time window, as can be within 50K temperature, the dark exciton radiative recombination starts to fall, and bright exciton dominates the emission mechanism. Looking at the carrier population taking part in these transitions in both time window, at T=300K, all the emission is coming from bright states with short lifetime. Hence, the lifetime observed would be in ns in 300K while the lifetime observed

would be in μs in 15K temperature. This has been previously reported for 4nm size GeSn quantum dots as discussed in section 2.2. The quantum yield estimated for this system is 25% and 19% for Sn concentration variation from 2.4% to 5.9%. If we compare to the activation energies obtained for the ~4nm dots as discussed in section 3.1, higher Sn content and larger size results in more non-radiative channels in the core which could lead to more non-radiative channels. This is reflected in the reduction in activation energy observed in the fit to experimental data and in this model by the lower values of E_{nD}, E_{nT} and E_2.

In conclusion, this theoretical model can to a reasonable degree of accuracy account for the carrier dynamics that were observed in investigations of the different size and composition of GeSn QD. The PL quenching and PL peak position change can be accounted for by change in initial trap state population, change in the energy levels with temperature along with change in carrier population due to trapping and de-trapping of carrier from surface trap states.

4. GeSiSn Alloy: Carrier Dynamics Model, Results and Discussion

The GeSn QD's explored so far have range of spectrum that spans from visible to near-infrared. As was discussed before even ultra-small QD's demonstrated so far are unable to extend the wavelength anymore beyond the visible in the shorter wavelength range (2.0 eV). So, Silicon incorporation can allow to extend to the short UV range in these quantum confined structures. In this chapter, first section will discuss aim to establish a background of Si QD system and GeSiSn alloy. Later sections will extend the rate equation model developed in Chapter 3, section 3.2 to GeSiSn model to aim to gain insight into behavior of the system with change in temperature.

4.1 Background- Si nanocrystals and GeSiSn alloy

Si is an indirect semiconductor that has a higher bandgap (1.12 eV) and a smaller lattice constant (5.43 Å) compared to both bulk Ge (0.67eV, 5.65Å) and Sn (0.08eV, 6.49Å). Although GeSn and GeSi systems of alloys have been widely explored, GeSiSn based alloys have been subjected to limited investigation. It has been explored as a potential IR semiconductor that can be used as active layers in optoelectronic devices via band gap tuning. It can also be used as a structural buffer for the integration of dissimilar compounds with silicon. In alloy form, it also presents a realistic opportunity for achieving independent strain and band structure manipulation in group IV materials. Temperature dependent photoluminescence studies have demonstrated that, bandgap of GeSiSn ternary alloy clearly increases after Si incorporation into GeSn.

Silicon is a group IV material known for its abundant use in microelectronic devices [74, 75] and also has been used in different optoelectronic devices such as photovoltaic cell and photodetectors.[76, 77] Silicon is generally not regarded as a material of choice for optoelectronics due to its indirect bandgap and as a result integrating both optical and electrical functions on a silicon based chip is both a challenge and a widely sought after target as it will unveil a plethora of integration option to existing platforms. Development of silicon based emitters has started in

the beginning with porous silicon structures [78, 79] and then gradually moved to silicon quantum wells and superlattices [80-82], nanowires and finally to nanocrystals and quantum dots[83-86].

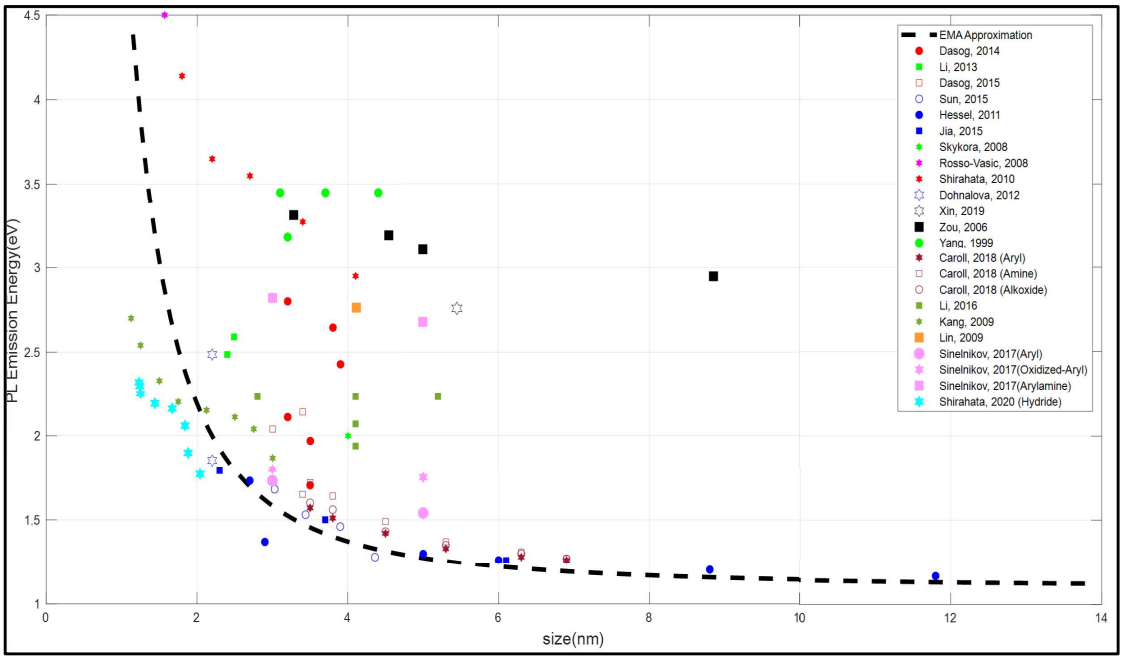

Figure 4.1: PL peak emission versus Si nanocrystal diameter

The relation between size of Si nanocrystal and energy gap for various methods of synthesis over the years is given in Figure 4.2. The energy gap of the experimental data is from PL emission of silicon nanocrystals dispersed in solutions and the theoretical estimation is obtained the change of quantum confinement with change in size as described by Equation 1 from Chapter 1. As you gradually change the size of a material from bulk to that of close to its excitonic Bohr radius, the material loses its characteristic continuous band structure. The density of states changes from continuous to discrete and the energy gap increases causing a blue shift in the absorption and emission spectra enhancing the direct transition rates in the materials and this can be utilized to enhance emission from silicon[87]. Colloidal silicon nanocrystals and quantum dots offer added advantages such as low cost method of production, nontoxicity, bio-compatibility etc. Silicon is highly reactive to oxygen and hence capping with ligands is essential for getting good emission from silicon nanocrystals. Fabrication and synthesis methods, surface capping/ligands have shown to significantly alter the emission characteristics of silicon nanocrystals. Silicon nanocrystals

grown by high temperature nucleation of silicon from SiO, thermal decomposition of HSQ, non-thermal plasma assisted growth (mean diameter between 2 to 6 nm) have shown to be in good agreement with size and quantum confinement[88-90]. Most of these dots are passivated with alkene ligands.

Change in surface structure, ligand passivation causes significant changes on Si nanoparticle emission properties. Change in surface chemistry can lead to introduction of surface states which can act as trap centers and even recombination centers for electron, holes, and excitons. This leads to change in emission characteristics of the nanoparticle. Surface can be modified by using a variety of ligands in the case of Silicon nanocrystals. Silicon quantum dots that are with organic (decyl group) that is long chain carbon based ligands and hydride based passivation have generally shown emission characteristics that follow predicted emission due to quantum confinement of the core. Caroll et al. [91] demonstrated hydride terminated silicon nanocrystals that were prepared using non-thermal RF plasma and functionalized with alkyls, amides and alkoxide. All three ligand passivated nanocrystals showed change in PL peak emission energy with size as the size of the nanocrystals was varied from 3.5 nm to 6.5 nm. Dasog et al.[92] demonstrated tuning of Silicon nanoparticle emission colors from blue to green without any size dependence by changing the surface ligands for 3-4nm size silicon nanocrystals. Emission was tuned in the spectral range of 1.53eV and 1.85eV. Li et al. [28] showed that, for colloidally synthesized Nitrogen capped silicon nanocrystals, strong emission arises from radiative recombination on the surface nitrogen sites and these tend to show no noticeable dependence on size as the size was changed from 4.8nm to 2.8nm and gave a strong yellow emission. Emissions from Nitrogen based surface states however depends on the type and structure of the ligand and can thus different N_2 groups tend to tune emission properties of Silicon nanoparticles [93, 94] differently. These Si nanoparticles with different nitrogen based surface ligands such as 4-aminoacetophenone, phenyl-1,4-phenylenediamine

groups have demonstrated shift in the emission from blue to red when excited with a source of 400 nm and showed no size dependence. The degree of delocalization of the HOMO and LUMO can change as surface state energy levels mix with these trap states energy. This can cause the energy gap between them decrease due to the N_2 groups. In case of passivation with nitrogen based ligands, generally arylamine groups show a red shift in PL position while allylamines show emission in the blue range with nanosecond lifetimes. Halogen[95] and Oxygen[96] also plays a crucial role in determining the emission characteristics of silicon nanocrystals. Depending on the type and structure of bond formation by these materials along with crystallinity, synergetic effects with surface, it can vary widely. Gradual oxidation of red emitting QD's show slow decrease in red emission band(2.07eV) and a growing blue emission band(2.7eV) for 5-10 nm Si quantum dots and was a result of to the partial coverage of Si nanoparticles via different ligand groups and subsequent oxidation. To this end, blue to cyan emission has been observed for oxidized silicon nanoparticles that are treated in peroxides and usually have nanosecond lifetime[97, 98]. This has been attributed to decrease in core size because of oxidation.

As is clear from the discussion above, surface chemistry and size dependent emission from silicon based quantum dots have been well explored. Surface along with size undoubtedly places a significant role in the emission properties of silicon nanocrystals and quantum dots. Incorporation of Silicon into GeSn colloidal QD system hence offers not only a variety of methods to extend emission to shorter wavelength but also mechanisms to suppress the contribution of surface which can lead to enhanced emission from core of QD. This can be done by proper choice of colloidal synthesis method coupled with appropriate choice of passivating ligands. In the succeeding section of this chapter, the change in emission characteristics and carrier dynamics in GeSiSn would be discussed and rate equation model would be extended to this system to understand the observations and difference with GeSn based system.

4.2 Steady-state and time-resolved PL measurements

GeSiSn samples with Sn composition varying between 4% to 17% and Si composition varying between 6%, 16% and 24% was investigated with solid stated PL at room temperature and time resolved PL.

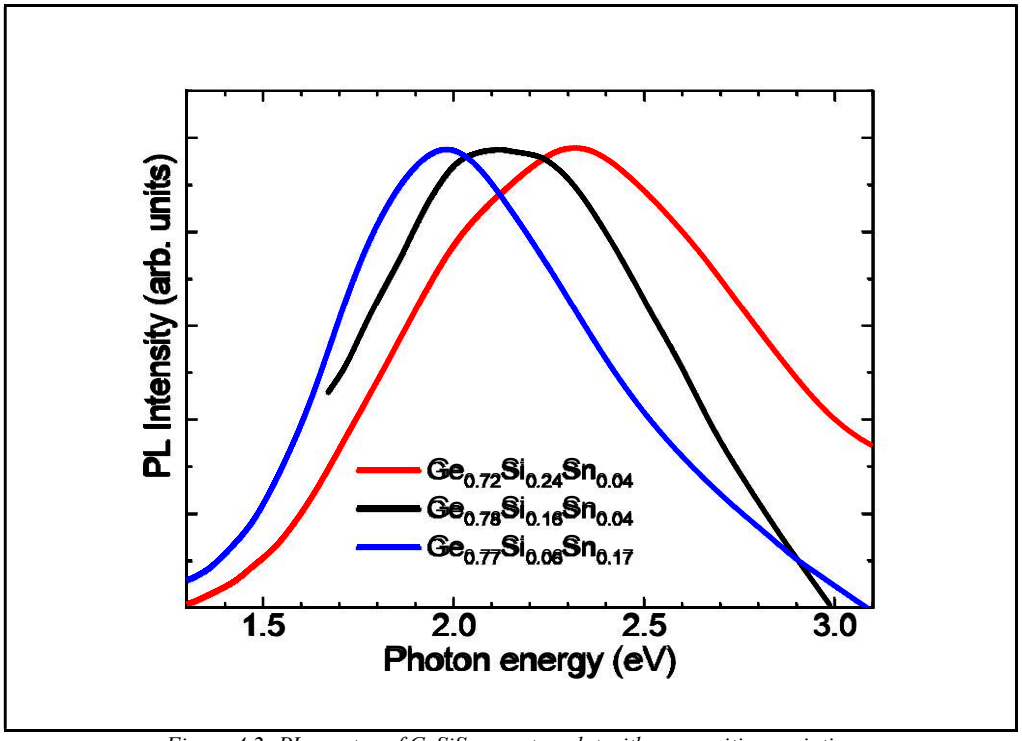

Figure 4.2: PL spectra of GeSiSn quantum dot with composition variation

The steady-state spectra of polydisperse Si-Ge-Sn alloy QDs (2–10 nm) of varying compositions are shown in the figure above. The blueshift in the PL spectrum is clear with increasing Si for samples having constant Sn or constant Ge content. When compared to the PL spectra of QDs in solution, the solid-state samples drop-casted on sapphire or silicon substrates exhibit redshifts as large as 250 meV. This could be a result of poorer passivation of QDs in the solid-state, which leaves particularly the smallest particles non-emissive. Si has larger effect on the bandgap if we compare the sample with composition of Sn varies from 4% to 17%, there is still clear blueshift with increase in Sn composition and PL peak position moves from 1.8 eV to 2.4 eV. Compared to GeSn samples with 12.5% Sn composition there is a blue shift in PL peak

position with even as little as 6% Si incorporation. Theoretically, Si is smaller than all the other constituent elements, it tends to compensate the effect in the strain in the Ge lattice due to Sn. This should potentially decrease the effect of Sn. Since the bandgap in Si is larger than in Ge or Sn, the energy gap is reduction due to addition of Sn does not have significant effect when it is coupled with the quantum confinement. This could as a secondary effect lead to possible reduction in performance from QD with inclusion of Si, but oscillator strength is increased due to incorporation of Sn. Therefore, by adding Sn to the binary alloy and varying Sn and Si content, a wider range of energies in the visible become accessible, while maintaining strong oscillator strengths. This could account for small amounts of Si addition causing significant change on PL peak emission that is observed in this ternary alloy QD.

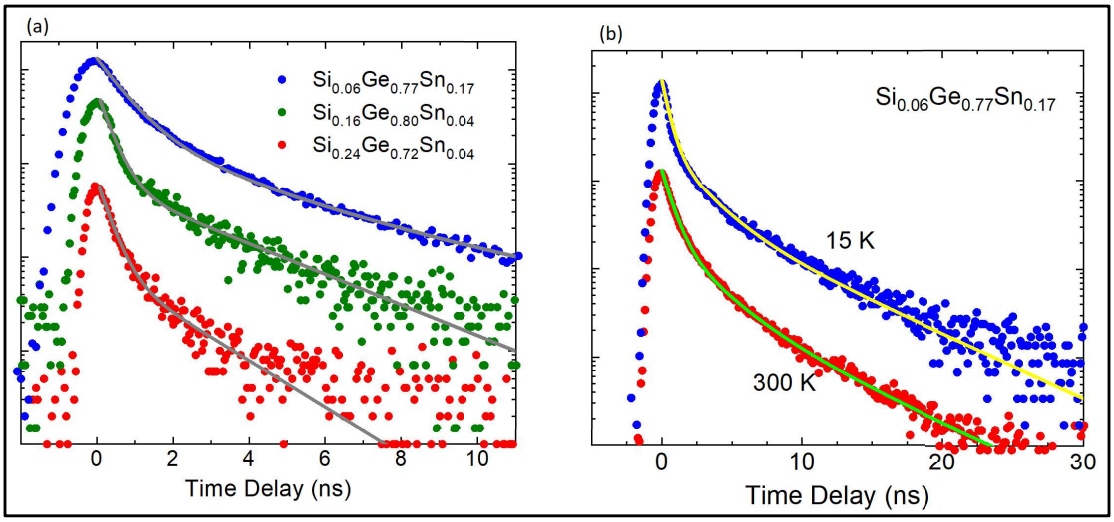

Figure 4.3: (a) TRPL spectra of GeSiSn quantum dot with composition variation (b) TRPL of GeSiSn with Sn composition 17% and Si composition 6% at 300K and 15K

TRPL decays in $Ge_{1-x-y}Si_xSn_y$ QDs also reveal some distinct features as shown in Figure 4.4 (a) and (b). The decay of photoluminescence with time is biexponential in nature and decay constants from the TRPL was obtained by using a fitting given below,

$$I_{TRPL} = A_{slow}e^{-\frac{t}{\tau_{slow}}} + A_{fast}e^{-\frac{t}{\tau_{fast}}}$$

The slow decay components at room temperature are in the order of 2 to 3ns. It is almost

independent of the temperature and only show slight increase when Silicon composition changes from 2,17ns to 3.13ns when Si composition changes from 6% to 24%. GeSn quantum dots had decay constants in the order of 8 to 12ns for similar Sn composition. The 15K data shows a slow decay constant on the order of 5.03ns. This behavior is drastically different when compared to $Ge_{1-x}Sn_x$ QDs, which exhibited ~20 μs PL decay times at 15 K, due to slow recombination of dark excitons and carriers localized at surface traps, suggesting vastly different carrier dynamics in ternary QDs. The results also are different from the decay characteristics found in GeSi self-assembled QD's on silicon which show change in photo-induced absorption to change from 3μs to 25μs for change in temperature from 270K to 80K[99].

To extend the carrier dynamic model established in previous section, certain changes were made to the existing model and the results is shown in the figure 4.5. Here the LO phono energy is kept equal to the energy in GeSi alloy[100]. The model is simplified by β parameter equal to the value of Germanium LO phonons. The values of the parameters were obtained after simulation is listed in Table 6.

Table 6: *Parameters for fit to PL decay for GeSiSn QD*

E_{ph}	**$\kappa_b(s^{-1})$**	**$\kappa_d(s^{-1})$**		**$k_o(s^{-1})$**	**Δ_{DB} (eV)**	***B(K)***	
34.6	$\frac{1}{1.5\times10^{-9}}$	$\frac{1}{2\times10^{-9}}$		$\frac{1}{4\times10^{-9}}$	2	290	
E_1 (meV)	**E_2 (meV)**	**E_{dis} (meV)**	**E_{esc} (meV)**	**E_{nD} (meV)**	**E_{nT} (meV)**	**α_b (meV/K)**	**α_d (meV/K)**
57±11.6	89.2±7.8	30.23±3.9	37±9.0	27±1.3	20 ± 2.6	0.001±9.0	0.009±9.0

The values for bright and dark exciton decay rate was kept constant as outlined in previous chapters based on GeSn system and k_o and n_{trap} was obtained from uniqueness plots and 50% value for n_{trap} was set (See Appendix A3). As can be seen from the simulation, significant decrease in the value

bright and dark exciton splitting is observed. Initial value of exciton splitting was taken to be 2 meV at 15K. This makes it possible for bright excitons to be populated even at exceptionally low temperatures which is why both 15K and 300K time decay is observed to be on the ns range. E_1 and E_2 values are comparable to the values obtained for GeSn systems. The biggest contribution to the PL decay comes from the value of splitting itself. It is known that inclusion of Sn causes lowering of the exciton splitting level, there could be further lowering with inclusion of Si into the system that could account for the ns delay. In most semiconductor QD systems like CdS, PbS, Si at least an order of magnitude change in decay constant is usually observed with change in temperature[51, 101, 102].

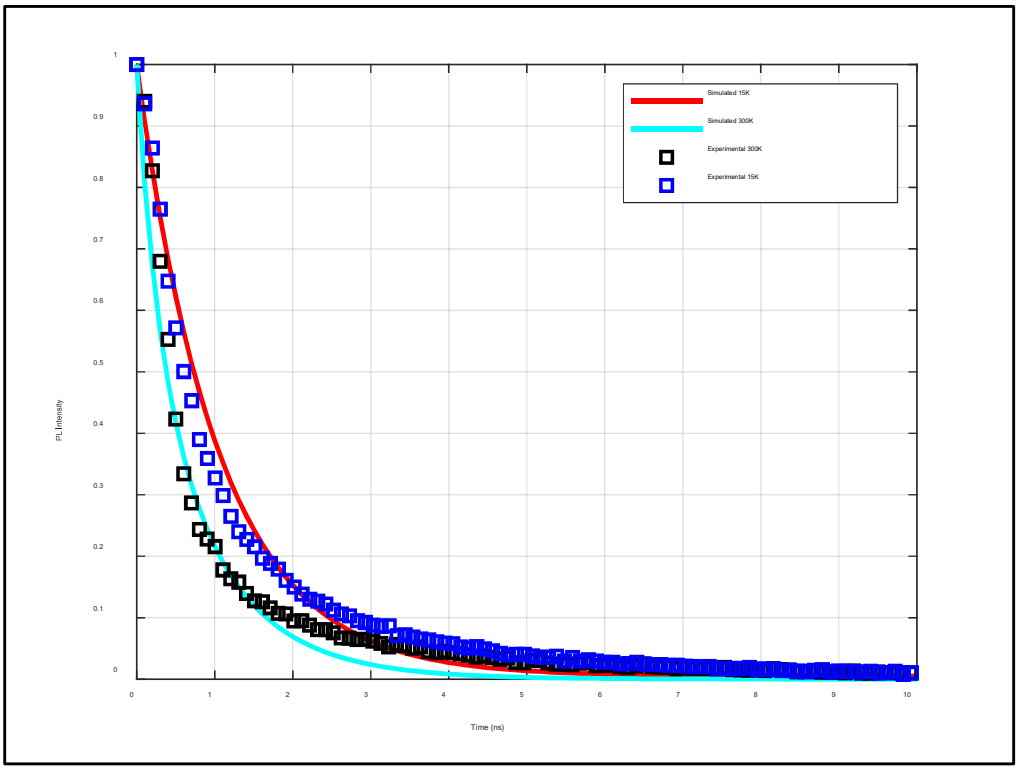

Figure 4.4: Experimental and simulated decay characteristics obtained from Theoretical model

Figure 4.4 shows the simulated and experimental data plotted together for GeSiSn with 17% Sn and 6% Si. The goodness of varies by 10% within the bounds. The RMSE for the fits at 15K and 300K are calculated to be 0.15 and 0.29. The change in PL peak position as well as the

integrated PL intensity can also be obtained from the theoretical model. The obtained results are shown in Figure 4.5. As can be seen the PL has a sharp fall beyond 50K temperature. This could be due to exciton dissociation. Also, there is trap related non-radiative recombination channels that are activated post 50K. The model estimates the value of trap states and recombination channel being lower so there is possibility of significant reduction in PL intensity going from 15K to 300K. Quantum yield was estimated to be around 15% for this sample and will likely be in the lower range in actual sample as only two channels were considered here. The PL position does not show much variation. This could be due to the bright excitons being activated at very low temperatures combined with low values of lowering of the energy levels. This is clearly a significant outcome of Si incorporation as it gives stability to emission wavelength and suppresses change in emission wavelength with change in device temperature. This is a desired property in many light emitting devices.

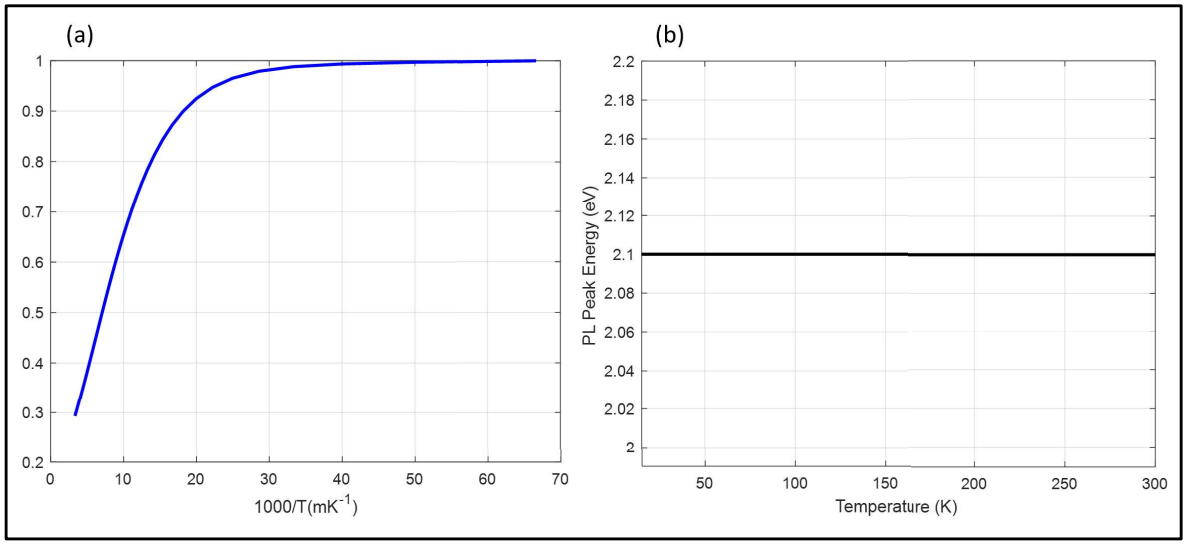

Figure 4.6: (a) Integrated PL Intensity (b) Change in PL Peak Position with temperature obtained from Theoretical Modelling

It can be concluded from this discussion that Silicon incorporation can both extend operational range of wavelength for the QD system but also allow for amazingly fast radiative recombination at both low and high temperatures with insignificant change in energy of PL peak emission which in turn will enhance the efficiency of the system.

5. Conclusion and Future Prospect

In the thesis, $Ge_{1-x}Sn_x$ QDs and GeSiSn QDs were investigated using a set of experimental techniques such as PL, TRPL and a theoretical model was established to explore the nature and characteristics of recombination dynamics in these colloidal systems. GeSn and GeSiSn QDs are still in research phase in terms of production but shows great potential for integration with existing semiconductor platforms and as a material for optoelectronic device fabrication. To make inroads into device applications, the QDs explored here require proper passivation, narrow size dispersity and uniform incorporation of Sn and Si. These nanoparticles have the added advantage due to facile, low cost method of synthesis using fast colloidal chemistry and their non-toxicity. This thesis has aimed to explore the physics of carrier dynamics to predict behavior of the QD system with change in temperature and composition. Here, temperature dependent change in carrier dynamics in colloidally synthesized 2 nm sized $Ge_{1-x}Sn_x$ QDs (x = 0.055, 0.066) and 4nm sized QDs (x = 0.0243, 0.0586) haves been investigated and PL decay times were found to be μs range at 15 K due to surface traps and the slow recombination of spin forbidden dark excitons. At room temperature, they decreased to nano second range and this dramatic change was attributed to the effect of spin-allowed bright excitons. The transition occurs at a temperature of ~200K and surface trap state concentration, radiative recombination from bright, dark and trap states along with non-radiative channels contribute to gradual blue shift in 2nm sized QDs and result in negligible shift in larger QDs. With 4nm dots, there was no observable changes in PL peak position energy. Using a rate equation model with dark, bright and trap states, carrier distribution in between the states with change in temperature, the shift observed in PL peak position and PL quenching has been explained. It is also estimated from the model that in 4nm QD system, the reduction in confinement tends to give access to more non radiative channels in them. Depending on the size of the quantum dot being investigated, surface trap states and the change in exciton and bright and dark level are

drastically different. This directly contributes to the difference in temperature dependent PL peak position change as well as decay dynamics. Aging and exposure to air also over a long period of time can affect these quantum dot systems. In the future, systematic aging studies can be explored to understand the long term characteristics of the system.

Incorporation of silicon was also investigated and the carrier dynamic model was extended to the ternary GeSiSn system to reveal drastically different high and low temperature carrier dynamics that could be due to dramatic decrease in exciton splitting energy as a result of both Sn and Si incorporation into the quantum dot system as well as faster relaxation rate for carrier exchange among different states. It also indicates that GeSiSn system should show little red shift to no change in PL peak emission with change in temperature which could be an extremely useful property in terms of device application.

Understanding the temperature dependent exciton dynamics of group IV alloy QD system uncovers a variety of opportunity in the future to apply these nanoparticles in devices. These devices can be manufactured through use of layers of QD thin film matrices. There are however several challenges that exist to achieve this end. Nanoparticles need to be well passivated through different types of ligands. But ligands being organic long chain molecules are detrimental to charge transport that is necessary for proper functioning of the device. Efficient and bright QD based light emitting devices need to have optimized excitonic confinement combined with excellent charge transport. One approach could be engineering the solution processed colloidal quantum dots (CQD) to have graded composition outer layer that suppresses recombination at surface[103] in a core-shell structure. Another approach is exchanging organic ligands completely with short, transport-compatible inorganic ligands[104, 105]. The ligand binding energies, before and after the exchange is significantly different and is primarily determined by the composition of the surface of the CQD. Due to distinct surface energy of different colloidal QDs, it is hard to

implement. However, some research groups have already shown success in implementing ligand exchange that retains both confinement and allows high transport[104].These methods make the passivation of QDs and later ligand exchange possible both in solution and in solid state. These QDs can then be spin coated on suitable substrates. Additional solution processed QD layers can be used to aid electron and hole injection and/or transport in the active layer of the device and then electric contact is patterned on these structures for fabrication of for example light emitting devices or photodetectors. One approach is illustrated in Figure 5.1.

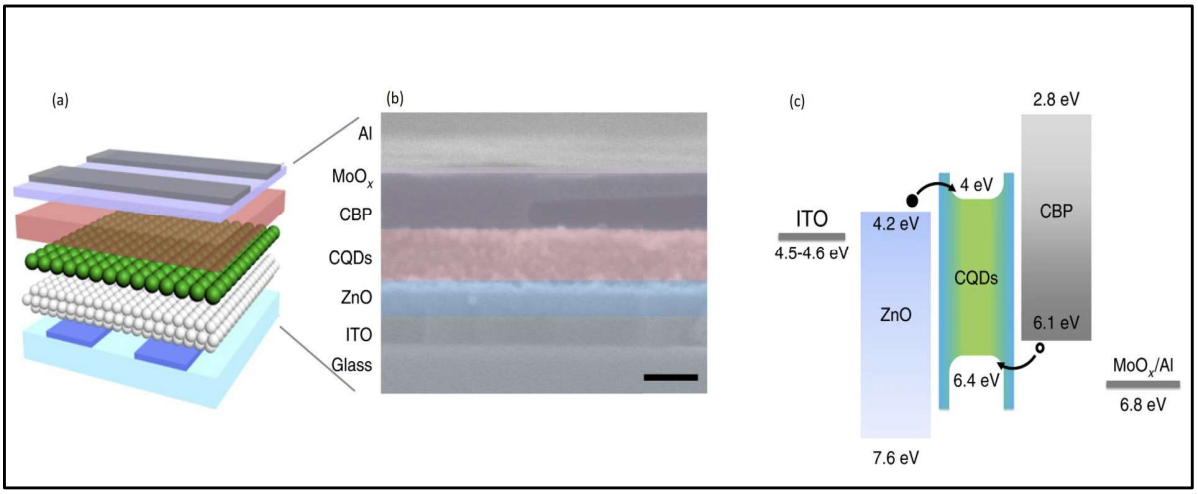

Figure 5.1: Zn chalcogenide-shelled colloidal quantum dots (a) A schematic representation (b) cross-sectional TEM image (right) of the inverted QLED (c) its energy band diagram in the unbiased condition. Contrary to a conventional device structure, the electrons are injected from ITO, while holes are injected from Al in this inverted structure. Chlorination the carboxylic group of oleic acid ligands results in grafting of the surfaces of the colloidal quantum dots with passivating chloride anions. Improved mobility that retain high external quantum efficiencies in the high-injection-current region and a reduced turn-on voltage of 2.5 V is observed as a result. (Li, et al. Nature Photonics, 2018)

A different way to accomplish the same goal could be is to take advantage of the naturally occurring high density of trap states instead of passivation for fabrication of QD photodetectors. Multiple trappings and release transport dynamics in band tail states exist in these CQDs. High performance can be achieved by allowing carriers to be swept to the electrodes before they fall into the band tail states using sandwich microstrip transmission line photodetector[106]. It was demonstrated by Gao, et al. and the device schematic is illustrated in Figure 5.2. Potential for extending CQD film to different types of optoelectronic technology is nothing short of groundbreaking. In addition to LED's, photodetectors large area all-solution based manufacture of

thin-film solar cells are possible. Ligand exchange can be employed to improve sub bandgap trap states that can greatly enhance both power conversion efficiency and air stability[107].

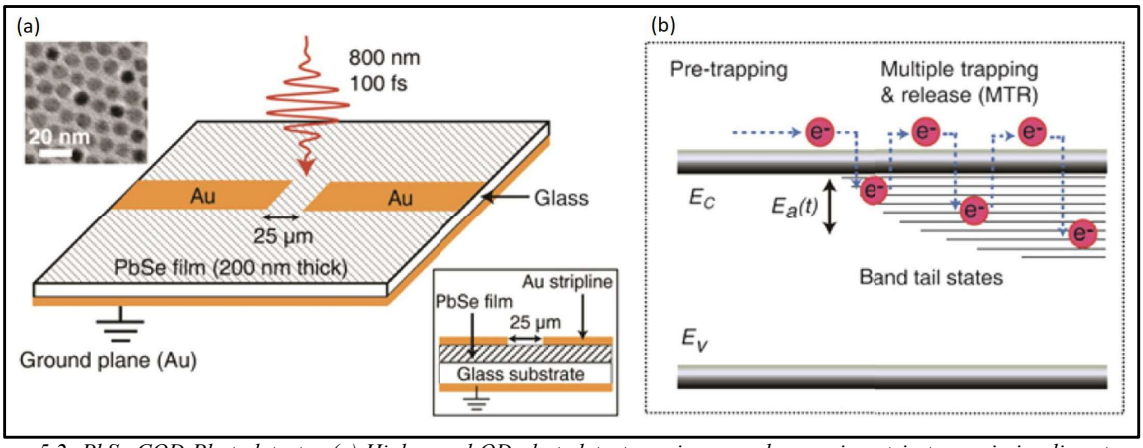

Figure 5.2: PbSe CQD Photodetector (a) High-speed QD photodetector using a coplanar microstrip transmission line structure (b) Scheme of multiple trap and release transport dynamics in the band tail states, illustrating that activation $E_a(t)$ increases with longer delay time after photoexcitation, as the charges fall into deeper traps over time. A similar transport dynamics model is also applied to the hole carrier in the band tail states. (Gao, et al. ACS Photonics. 2017)

Quantum dot buffer layer at the junction between thin film quantum dot active region layers can be utilized in these solar cells. Surface and size-tunable electronic properties of different quantum dots can be optimized to this end to improve its carrier concentration and energy band alignment in heterojunction solar cell structurers[108] and the device structure developed by Zhao, et al. is being shown in Figure 5.3.

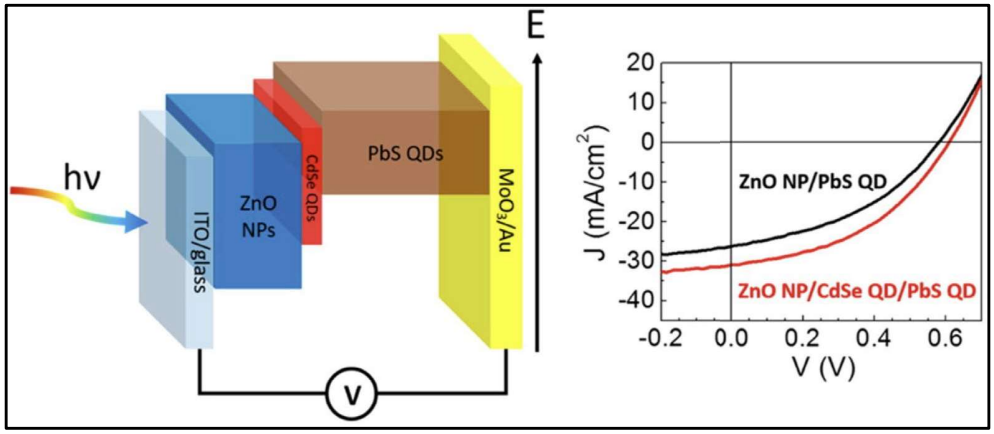

Figure 5.3: PbS QD solar cells by introducing a CdI_2–CdSe QD buffer layer at the ZnO NP/PbS QD heterojunction. (a) Schematic of Device Structure (b) Current density–voltage (J–V) characteristics of representative solar cells without (black) and with (red) a CdSe QD buffer layer under AM 1.5 illumination. (Zhao, et al. ACS nano. 2016)

In summary, QD thin film layers can be used in many ways to produce efficient optoelectronics devices. The investigations performed in this thesis aim to understand the physics behind the

behaviors observed in the binary and ternary group IV alloy system with change in material composition and size. Valuable insight about possible effect of surface traps, change of energy levels as wells exciton splitting energy is obtained here that can be used to make effective and efficient light emitting devices with colloidally synthesized QD thin films. Ease of integration of optoelectronic component into Silicon platforms using this alloy system makes it even more attractive as a possible light emitting material. Along with the results presented here, further investigations into the carrier dynamics, emission properties and charge transfer characteristics are necessary to fully utilize the scope of these nanoparticles and quantum dots to produce reliable, reproducible, low cost light emitting devices.

Appendix A

A.1: Uniqueness Plot of MSE for 2nm $Ge_{1-x}Sn_x$ QD (6.6% Sn)

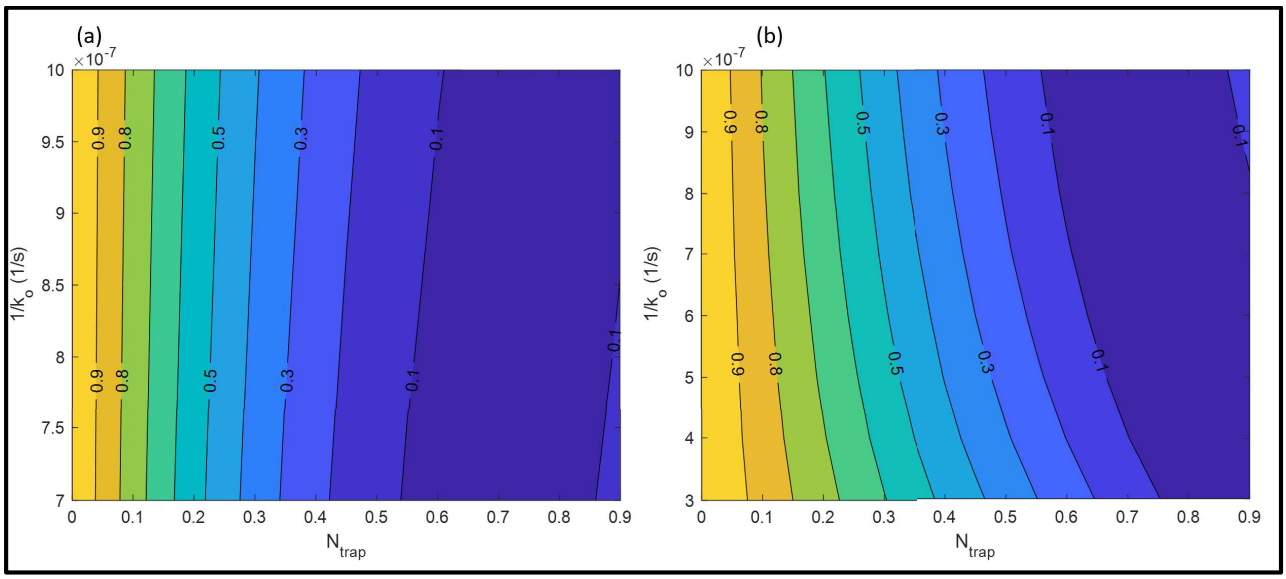

Figure A1: Uniqueness plots for change in Mean square error in the fits of (a) Integrated PL Intensity and (b) PL peak position as a function of the initial trap concentration for ultra-small (~2nm) $Ge_{1-x}Sn_x$ with 6.6% Sn.

A.2: Uniqueness Plot of MSE 4nm $Ge_{1-x}Sn_x$ QD (5.9% Sn)

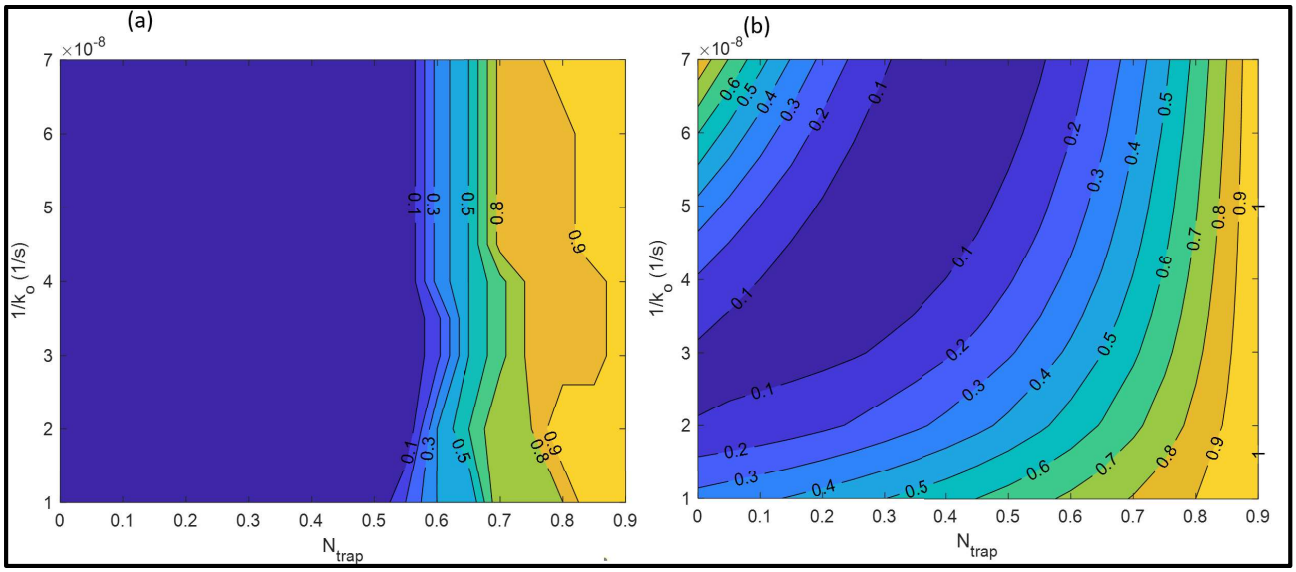

Figure A2: Uniqueness plots for change in Mean square error in the fits of (a) Integrated PL Intensity and (b) PL peak position as a function of the initial trap concentration for larger (~4nm) $Ge_{1-x}Sn_x$ with 5.9% Sn.

A.3: Uniqueness Plot of MSE for $Ge_{1-x-y}Si_ySn_x$ QD (17% Sn and 6% Si)

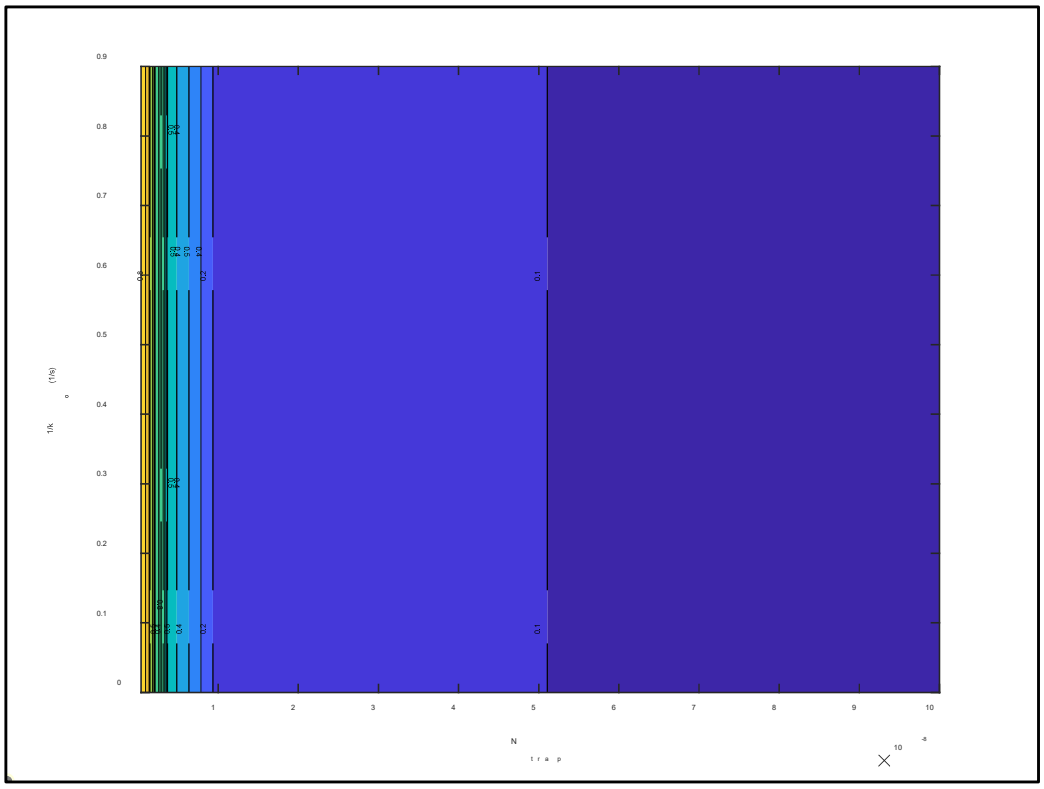

Figure A3: Uniqueness plots for change in Mean square error in the fits of TRPL of $Ge_{1-x-y}Si_ySn_x$ at 15K as a function of trap Concentration and k_o.

A.4: Goodness of Fit for Binary Alloy QD ($Ge_{1-x}Sn_x$)

Composition, x% (size, nm)	Integrated PL Intensity Curve Fit	PL Peak Intensity Curve Fit
	RMSE	RMSE
5.5% (2nm)	0.092	0.013
6.6% (2nm)	0.084	0.016
2.4% (4nm)	0.05	0.007
5.9% (4nm)	0.14	0.015

List of References:

1. Ahn D, Hong C-y, Liu J, Giziewicz W, Beals M, Kimerling LC, et al. High performance, waveguide integrated Ge photodetectors. Optics express. 2007;15(7):3916-21.
2. Cheng S-L, Lu J, Shambat G, Yu H-Y, Saraswat K, Vuckovic J, et al. Room temperature 1.6 μm electroluminescence from Ge light emitting diode on Si substrate. Optics Express. 2009;17(12):10019-24.
3. Michel J, Liu J, Kimerling LC. High-performance Ge-on-Si photodetectors. Nature photonics. 2010;4(8):527-34.
4. Oehme M, Werner J, Gollhofer M, Schmid M, Kaschel M, Kasper E, et al. Room-temperature electroluminescence from GeSn light-emitting pin diodes on Si. IEEE Photonics Technology Letters. 2011;23(23):1751-3.
5. Han J, Tan M, Zhu J, Meng S, Wang B, Mu S, et al. Photovoltaic characteristics of amorphous silicon solar cells using boron doped tetrahedral amorphous carbon films as p-type window materials. Applied physics letters. 2007;90(8):083508.
6. Crabb R, Treble F. Thin silicon solar cells for large flexible arrays. Nature. 1967;213(5082):1223-4.
7. Wang X, Cheng Z, Xu K, Tsang HK, Xu J-B. High-responsivity graphene/silicon-heterostructure waveguide photodetectors. Nature Photonics. 2013;7(11):888-91.
8. Jancu J-M, Scholz R, Beltram F, Bassani F. Empirical spds* tight-binding calculation for cubic semiconductors: General method and material parameters. Physical Review B. 1998;57(11):6493.
9. El Kurdi M, Bertin H, Martincic E, De Kersauson M, Fishman G, Sauvage S, et al. Control of direct band gap emission of bulk germanium by mechanical tensile strain. Applied Physics Letters. 2010;96(4):041909.
10. Boztug C, Sánchez-Pérez JR, Cavallo F, Lagally MG, Paiella R. Strained-germanium nanostructures for infrared photonics. ACS nano. 2014;8(4):3136-51.
11. Sukhdeo DS, Nam D, Kang J-H, Brongersma ML, Saraswat KC. Direct bandgap germanium-on-silicon inferred from 5.7%⟨ 100⟩ uniaxial tensile strain. Photonics Research. 2014;2(3):A8-A13.
12. Süess MJ, Geiger R, Minamisawa R, Schiefler G, Frigerio J, Chrastina D, et al. Analysis of enhanced light emission from highly strained germanium microbridges. Nature Photonics. 2013;7(6):466-72.
13. Gassenq A, Guilloy K, Osvaldo Dias G, Pauc N, Rouchon D, Hartmann J-M, et al. 1.9% bi-axial tensile strain in thick germanium suspended membranes fabricated in optical germanium-on-insulator substrates for laser applications. Applied Physics Letters. 2015;107(19):191904.
14. He G, Atwater HA. Interband transitions in Sn x Ge 1− x alloys. Physical review letters. 1997;79(10):1937.
15. Moontragoon P, Ikonić Z, Harrison P. Band structure calculations of Si–Ge–Sn alloys: achieving direct band gap materials. Semiconductor science and technology. 2007;22(7):742.
16. Du W, Ghetmiri SA, Conley BR, Mosleh A, Nazzal A, Soref RA, et al. Competition of optical transitions between direct and indirect bandgaps in Ge1− xSnx. Applied Physics Letters. 2014;105(5):051104.
17. Gupta S, Magyari-Köpe B, Nishi Y, Saraswat KC. Achieving direct band gap in germanium through integration of Sn alloying and external strain. Journal of Applied Physics. 2013;113(7):073707.
18. Yin W-J, Gong X-G, Wei S-H. Origin of the unusually large band-gap bowing and the breakdown of the band-edge distribution rule in the Sn x Ge 1− x alloys. Physical Review B. 2008;78(16):161203.
19. Gupta S, Chen R, Magyari-Kope B, Lin H, Yang B, Nainani A, et al., editors. GeSn technology: Extending the Ge electronics roadmap. 2011 International Electron Devices Meeting; 2011: IEEE.
20. Chen R, Lin H, Huo Y, Hitzman C, Kamins TI, Harris JS. Increased photoluminescence of strain-reduced, high-Sn composition Ge1− x Sn x alloys grown by molecular beam epitaxy. Applied physics letters. 2011;99(18):181125.
21. Grzybowski G, Beeler R, Jiang L, Smith D, Kouvetakis J, Menendez J. Next generation of Ge1− y

Sn y (y= 0.01-0.09) alloys grown on Si (100) via Ge3H8 and SnD4: Reaction kinetics and tunable emission. Applied physics letters. 2012;101(7):072105.
22. Seifner MS, Hernandez S, Bernardi J, Romano-Rodriguez A, Barth S. Pushing the Composition Limit of Anisotropic Ge1–x Sn x Nanostructures and Determination of Their Thermal Stability. Chemistry of Materials. 2017;29(22):9802-13.
23. Liu L, Liang R, Wang J, Xu J. Enhanced carrier mobility and direct tunneling probability of biaxially strained Ge1− x Sn x alloys for field-effect transistors applications. Journal of Applied Physics. 2015;117(18):184501.
24. Biswas S, Doherty J, Saladukha D, Ramasse Q, Majumdar D, Upmanyu M, et al. Non-equilibrium induction of tin in germanium: towards direct bandgap Ge 1− x Sn x nanowires. Nature communications. 2016;7(1):1-12.
25. Di Bartolomeo A, Passacantando M, Niu G, Schlykow V, Lupina G, Giubileo F, et al. Observation of field emission from GeSn nanoparticles epitaxially grown on silicon nanopillar arrays. Nanotechnology. 2016;27(48):485707.
26. Wang Y, Herron N. Nanometer-sized semiconductor clusters: materials synthesis, quantum size effects, and photophysical properties. The Journal of Physical Chemistry. 1991;95(2):525-32.
27. Silva FO, Carvalho MS, Mendonça R, Macedo WA, Balzuweit K, Reiss P, et al. Effect of surface ligands on the optical properties of aqueous soluble CdTe quantum dots. Nanoscale research letters. 2012;7(1):536.
28. Li Q, Luo T-Y, Zhou M, Abroshan H, Huang J, Kim HJ, et al. Silicon nanoparticles with surface nitrogen: 90% quantum yield with narrow luminescence bandwidth and the ligand structure based energy law. ACS nano. 2016;10(9):8385-93.
29. Reboredo F, Zunger A. Surface-passivation-induced optical changes in Ge quantum dots. Physical Review B. 2001;63(23):235314.
30. Xu F, Gerlein LF, Ma X, Haughn CR, Doty MF, Cloutier SG. Impact of different surface ligands on the optical properties of PbS quantum dot solids. Materials. 2015;8(4):1858-70.
31. Esteves RJA, Ho MQ, Arachchige IU. Nanocrystalline Group IV Alloy Semiconductors: Synthesis and Characterization of Ge1–x Sn x Quantum Dots for Tunable Bandgaps. Chemistry of Materials. 2015;27(5):1559-68.
32. Demchenko DO, Tallapally V, Esteves RJA, Hafiz S, Nakagawara TA, Arachchige IU, et al. Optical Transitions and Excitonic Properties of Ge1–x Sn x Alloy Quantum Dots. The Journal of Physical Chemistry C. 2017;121(33):18299-306.
33. Hafiz SA, Esteves RJA, Demchenko DO, Arachchige IU, Özgür Um. Energy Gap Tuning and Carrier Dynamics in Colloidal Ge1–x Sn x Quantum Dots. The journal of physical chemistry letters. 2016;7(17):3295-301.
34. Chibane Y, Ferhat M. Electronic structure of Sn x Ge 1− x alloys for small Sn compositions: Unusual structural and electronic properties. Journal of Applied Physics. 2010;107(5):053512.
35. Jain JR, Ly-Gagnon D-S, Balram KC, White JS, Brongersma ML, Miller DA, et al. Tensile-strained germanium-on-insulator substrate fabrication for silicon-compatible optoelectronics. Optical Materials Express. 2011;1(6):1121-6.
36. Fafard S, Wasilewski Z, Allen CN, Picard D, Spanner M, McCaffrey J, et al. Manipulating the energy levels of semiconductor quantum dots. Physical Review B. 1999;59(23):15368.
37. Alivisatos AP. Semiconductor clusters, nanocrystals, and quantum dots. science. 1996;271(5251):933-7.
38. Wuister SF, de Mello Donega C, Meijerink A. Influence of thiol capping on the exciton luminescence and decay kinetics of CdTe and CdSe quantum dots. The Journal of Physical Chemistry B. 2004;108(45):17393-7.
39. Sangghaleh F, Sychugov I, Yang Z, Veinot JG, Linnros J. Near-unity internal quantum efficiency of luminescent silicon nanocrystals with ligand passivation. ACS nano. 2015;9(7):7097-104.
40. Tallapally V, Nakagawara TA, Demchenko DO, Özgür Ü, Arachchige IU. Ge 1− x Sn x alloy quantum dots with composition-tunable energy gaps and near-infrared photoluminescence. Nanoscale.

2018;10(43):20296-305.
41. Ghetmiri SA, Du W, Margetis J, Mosleh A, Cousar L, Conley BR, et al. Direct-bandgap GeSn grown on silicon with 2230 nm photoluminescence. Applied Physics Letters. 2014;105(15):151109.
42. Ryu M-Y, Harris TR, Yeo Y, Beeler R, Kouvetakis J. Temperature-dependent photoluminescence of Ge/Si and Ge1-ySny/Si, indicating possible indirect-to-direct bandgap transition at lower Sn content. Applied Physics Letters. 2013;102(17):171908.
43. He G, Atwater HA. Synthesis of epitaxial Sn x Ge1− x alloy films by ion-assisted molecular beam epitaxy. Applied physics letters. 1996;68(5):664-6.
44. Ragan R, Min KS, Atwater HA. Direct energy gap group IV semiconductor alloys and quantum dot arrays in SnxGe1− x/Ge and SnxSi1− x/Si alloy systems. Materials Science and Engineering: B. 2001;87(3):204-13.
45. Kochereshkov V, Mikhailov G. Ural′ tsev, IN Magnetic field reversal at polaritons. Sov Phys Solid State. 1983;25:439-44.
46. Scholes GD, Rumbles G. Excitons in nanoscale systems. Materials For Sustainable Energy: A Collection of Peer-Reviewed Research and Review Articles from Nature Publishing Group: World Scientific; 2011. p. 12-25.
47. Norris DJ, Efros AL, Rosen M, Bawendi MG. Size dependence of exciton fine structure in CdSe quantum dots. Physical Review B. 1996;53(24):16347.
48. Robel I, Shabaev A, Lee DC, Schaller RD, Pietryga JM, Crooker SA, et al. Temperature and magnetic-field dependence of radiative decay in colloidal germanium quantum dots. Nano letters. 2015;15(4):2685-92.
49. Esteves R, Hafiz S, Demchenko D, Ozgur U, Arachchige I, editors. Synthesis and photophysical characterization of ultra-small Ge1-xSnx quantum dots. ABSTRACTS OF PAPERS OF THE AMERICAN CHEMICAL SOCIETY; 2016: AMER CHEMICAL SOC 1155 16TH ST, NW, WASHINGTON, DC 20036 USA.
50. Jones M, Lo SS, Scholes GD. Quantitative modeling of the role of surface traps in CdSe/CdS/ZnS nanocrystal photoluminescence decay dynamics. Proceedings of the National Academy of Sciences. 2009;106(9):3011-6.
51. Kim D, Mishima T, Tomihira K, Nakayama M. Temperature dependence of photoluminescence dynamics in colloidal CdS quantum dots. The Journal of Physical Chemistry C. 2008;112(29):10668-73.
52. Valerini D, Creti A, Lomascolo M, Manna L, Cingolani R, Anni M. Temperature dependence of the photoluminescence properties of colloidal Cd Se⁄ Zn S core/shell quantum dots embedded in a polystyrene matrix. Physical Review B. 2005;71(23):235409.
53. Narayanaswamy A, Feiner L, Meijerink A, Van der Zaag P. The effect of temperature and dot size on the spectral properties of colloidal inp/zns core− shell quantum dots. ACS nano. 2009;3(9):2539-46.
54. Ji C, Zhang Y, Zhang T, Liu W, Zhang X, Shen H, et al. Temperature-dependent photoluminescence of Ag2Se quantum dots. The Journal of Physical Chemistry C. 2015;119(24):13841-6.
55. Gaponenko MS, Lutich AA, Tolstik NA, Onushchenko AA, Malyarevich AM, Petrov EP, et al. Temperature-dependent photoluminescence of PbS quantum dots in glass: Evidence of exciton state splitting and carrier trapping. Physical Review B. 2010;82(12):125320.
56. Gao J, Johnson JC. Charge trapping in bright and dark states of coupled PbS quantum dot films. ACS nano. 2012;6(4):3292-303.
57. Andreakou P, Brossard M, Li C, Bernechea M, Konstantatos G, Lagoudakis PG. Size-and temperature-dependent carrier dynamics in oleic acid capped PbS quantum dots. The Journal of Physical Chemistry C. 2013;117(4):1887-92.
58. Garro N, Cantarero A, Cardona M, Ruf T, Göbel A, Lin C, et al. Electron-phonon interaction at the direct gap of the copper halides. Solid state communications. 1996;98(1):27-30.
59. Artus L, Bertrand Y. Anomalous temperature dependence of fundamental gap of AgGaS2 and AgGaSe2 chalcopyrite compounds. Solid state communications. 1987;61(11):733-6.
60. Woo HC, Choi JW, Shin J, Chin S-H, Ann MH, Lee C-L. Temperature-dependent photoluminescence of CH3NH3PbBr3 perovskite quantum dots and bulk counterparts. The Journal of

Physical Chemistry Letters. 2018;9(14):4066-74.
61. Zaima S, Nakatsuka O, Taoka N, Kurosawa M, Takeuchi W, Sakashita M. Growth and applications of GeSn-related group-IV semiconductor materials. Science and technology of advanced materials. 2015;16(4):043502.
62. Zhou T, Zhong Z. Optical properties demonstrating strong coupling of compactly arranged Ge quantum dots. Optics express. 2019;27(16):22173-80.
63. Kalytchuk S, Zhovtiuk O, Kershaw SV, Zbořil R, Rogach AL. Temperature-dependent exciton and trap-related photoluminescence of CdTe quantum dots embedded in a NaCl matrix: implication in thermometry. Small. 2016;12(4):466-76.
64. Morello G, De Giorgi M, Kudera S, Manna L, Cingolani R, Anni M. Temperature and size dependence of nonradiative relaxation and exciton− phonon coupling in colloidal CdTe quantum dots. The Journal of Physical Chemistry C. 2007;111(16):5846-9.
65. Giri P, Kesavamoorthy R, Panigrahi B, Nair K. Evidence for fast decay dynamics of the photoluminescence from Ge nanocrystals embedded in SiO2. Solid state communications. 2005;133(4):229-34.
66. Wang W, Li Y, Wang X, Liu Y, Lv Y, Wang S, et al. Interplay between Exciton and Free Carriers in Organolead Perovskite Films. Scientific reports. 2017;7(1):1-6.
67. Mayer A, Lightowlers E. Accurate determination of the exciton energy gap and the LA and LO momentum-conserving phonon energies in germanium. Journal of Physics C: Solid State Physics. 1979;12(13):L507.
68. Haines M, Cavenett B, Davey S. Optical phonon energies in pseudomorphic alloy strained layers. Applied physics letters. 1989;55(9):849-51.
69. Tang K, Wang T, Qi W, Li Y. Debye temperature for binary alloys and its relationship with cohesive energy. Physica B: Condensed Matter. 2018;531:95-101.
70. Allahverdi Ç, Yükselici M. Temperature dependence of absorption band edge of CdTe nanocrystals in glass. New Journal of Physics. 2008;10(10):103029.
71. Joshi A, Narsingi K, Manasreh M, Davis E, Weaver B. Temperature dependence of the band gap of colloidal Cd Se⁄Zn S core/shell nanocrystals embedded into an ultraviolet curable resin. Applied physics letters. 2006;89(13):131907.
72. Luo J, Franceschetti A, Zunger A. Nonmonotonic size dependence of the dark/bright exciton splitting in GaAs nanocrystals. Physical Review B. 2009;79(20):201301.
73. Franceschetti A, Zunger A. Direct pseudopotential calculation of exciton coulomb and exchange energies in semiconductor quantum dots. Physical review letters. 1997;78(5):915.
74. Venema L. Silicon electronics and beyond. Nature Publishing Group; 2011.
75. Hwang S-W, Tao H, Kim D-H, Cheng H, Song J-K, Rill E, et al. A physically transient form of silicon electronics. Science. 2012;337(6102):1640-4.
76. Casalino M, Coppola G, Iodice M, Rendina I, Sirleto L. Near-infrared sub-bandgap all-silicon photodetectors: state of the art and perspectives. Sensors. 2010;10(12):10571-600.
77. Rech B, Kluth O, Repmann T, Roschek T, Springer J, Müller J, et al. New materials and deposition techniques for highly efficient silicon thin film solar cells. Solar Energy Materials and Solar Cells. 2002;74(1-4):439-47.
78. Banerjee S, Narasimhan K, Ayyub P, Srivastava A, Sardesai A. Origin of luminescence in porous silicon. Solid state communications. 1992;84(6):691-3.
79. Gong M, Zeng C, Shi J, Wong W, Cheah K, Zheng W. Photoluminescence of porus silicon and praseodymium-doped porous silicon. CHINESE JOURNAL OF INORGANIC CHEMISTRY. 1999;15(1):29-34.
80. Zhen-guo J, Norikata U, Sunamura H, Yasuhiro S. Photoluminescence and Raman scattering of pure germanium/silicon short period superlattice. Acta Physica Sinica (Overseas Edition). 1998;7(8):608.
81. Saeta PN, Gallagher A. Photoluminescence properties of silicon quantum-well layers. Physical Review B. 1997;55(7):4563.
82. Zhu X, Lu J, Gao Y, Yuan S, Zhou N, Xie M, et al. Strong photoluminescence from ultrathin silicon

(110) quantum wells at room temperature. Japanese Journal of Applied Physics. 2017;56(2):020305.
83. Inoue A, Sugimoto H, Fujii M. Photoluminescence enhancement of silicon quantum dot monolayer by double resonance plasmonic substrate. The Journal of Physical Chemistry C. 2017;121(21):11609-15.
84. Balberg I, editor The Electrical Transport and Photoluminescence Mechanisms in Ensembles of Silicon Quantum Dots. AIP Conference Proceedings; 2009: American Institute of Physics.
85. Ghosh B, Takeguchi M, Nakamura J, Nemoto Y, Hamaoka T, Chandra S, et al. Origin of the photoluminescence quantum yields enhanced by alkane-termination of freestanding silicon nanocrystals: temperature-dependence of optical properties. Scientific reports. 2016;6(1):1-11.
86. Harriman TA, Lee JK, Sung GY, Lucca DA. Photoluminescence of Cerium Doped Si Nanocrystals Embedded in Silicon Nitride Films. physica status solidi (b). 2019;256(5):1800706.
87. Barbagiovanni EG, Lockwood DJ, Simpson PJ, Goncharova LV. Quantum confinement in Si and Ge nanostructures. Journal of Applied Physics. 2012;111(3):034307.
88. Sun W, Qian C, Wang L, Wei M, Mastronardi ML, Casillas G, et al. Switching-on quantum size effects in silicon nanocrystals. Advanced Materials. 2015;27(4):746-9.
89. Hessel CM, Reid D, Panthani MG, Rasch MR, Goodfellow BW, Wei J, et al. Synthesis of ligand-stabilized silicon nanocrystals with size-dependent photoluminescence spanning visible to near-infrared wavelengths. Chemistry of materials. 2012;24(2):393-401.
90. Jia X, Zhang P, Lin Z, Anthony R, Kortshagen U, Huang S, et al. Accurate determination of the size distribution of Si nanocrystals from PL spectra. RSC Advances. 2015;5(68):55119-25.
91. Carroll GM, Limpens R, Neale NR. Tuning confinement in colloidal silicon nanocrystals with saturated surface ligands. Nano letters. 2018;18(5):3118-24.
92. Dasog M, De los Reyes GB, Titova LV, Hegmann FA, Veinot JG. Size vs surface: tuning the photoluminescence of freestanding silicon nanocrystals across the visible spectrum via surface groups. ACS nano. 2014;8(9):9636-48.
93. Pi X, Chen X, Ma Y, Yang D. Optical absorption and emission of nitrogen-doped silicon nanocrystals. Nanoscale. 2011;3(11):4584-8.
94. Zhong Y, Sun X, Wang S, Peng F, Bao F, Su Y, et al. Facile, large-quantity synthesis of stable, tunable-color silicon nanoparticles and their application for long-term cellular imaging. ACS nano. 2015;9(6):5958-67.
95. Dasog M, Bader K, Veinot JG. Influence of halides on the optical properties of silicon quantum dots. Chemistry of Materials. 2015;27(4):1153-6.
96. Hua F, Erogbogbo F, Swihart MT, Ruckenstein E. Organically capped silicon nanoparticles with blue photoluminescence prepared by hydrosilylation followed by oxidation. Langmuir. 2006;22(9):4363-70.
97. Dohnalová K, Ondič L, Kůsová K, Pelant I, Rehspringer J, Mafouana R-R. White-emitting oxidized silicon nanocrystals: Discontinuity in spectral development with reducing size. Journal of Applied Physics. 2010;107(5):053102.
98. Gupta A, Wiggers H. Freestanding silicon quantum dots: origin of red and blue luminescence. Nanotechnology. 2010;22(5):055707.
99. Sofronov A, Vorobjev L, Firsov D, Balagula R, Tonkikh A, editors. Charge carrier kinetics in GeSi/Si quantum dots probed by mid-infrared radiation. Journal of Physics Conference Series (Online); 2017.
100. Logan RA, Rowell J, Trumbore F. Phonon spectra of Ge-Si alloys. Physical Review. 1964;136(6A):A1751.
101. Espiau de Lamaëstre R, Bernas H, Pacifici D, Franzo G, Priolo F. Evidence for a “dark exciton” state of PbS nanocrystals in a silicate glass. Applied physics letters. 2006;88(18):181115.
102. Julsgaard B, Lu Y-W, Balling P, Larsen AN. Thermalization of exciton states in silicon nanocrystals. Applied Physics Letters. 2009;95(18):183107.
103. Lim J, Park Y-S, Wu K, Yun HJ, Klimov VI. Droop-free colloidal quantum dot light-emitting diodes. Nano letters. 2018;18(10):6645-53.
104. Li X, Zhao Y-B, Fan F, Levina L, Liu M, Quintero-Bermudez R, et al. Bright colloidal quantum

dot light-emitting diodes enabled by efficient chlorination. Nature Photonics. 2018;12(3):159-64.
105. Kwak J, Bae WK, Lee D, Park I, Lim J, Park M, et al. Bright and efficient full-color colloidal quantum dot light-emitting diodes using an inverted device structure. Nano letters. 2012;12(5):2362-6.
106. Gao J, Nguyen SC, Bronstein ND, Alivisatos AP. Solution-processed, high-speed, and high-quantum-efficiency quantum dot infrared photodetectors. ACS photonics. 2016;3(7):1217-22.
107. Azmi R, Sinaga S, Aqoma H, Seo G, Ahn TK, Park M, et al. Highly efficient air-stable colloidal quantum dot solar cells by improved surface trap passivation. Nano Energy. 2017;39:86-94.
108. Zhao T, Goodwin ED, Guo J, Wang H, Diroll BT, Murray CB, et al. Advanced architecture for colloidal PbS quantum dot solar cells exploiting a CdSe quantum dot buffer layer. ACS nano. 2016;10(10):9267-73.

Vitae

Rahnuma Rahman was born on September 28, 1991, in the city of Dhaka, Bangladesh and is a citizen of Peoples Republic of Bangladesh. She graduated from Holy Cross Girls' High School and College located in Dhaka, Bangladesh in 2009. She received her Bachelor of Science in Electrical and Electronic Engineering from Bangladesh University of Engineering and Technology, Dhaka, Bangladesh in 2015. From 2015 to 2018, she has worked as a Lecturer in Department of Electrical and Electronic Engineering in Daffodil International University. With the completion of this thesis, in the Spring of 2020, she will receive her Master of Science in Electrical and Computer engineering from Virginia Commonwealth University.